DESIGN AND APPLICATIONS OF MINIMALLY INVASIVE ALL-POLE ANALOG FILTERS

A Thesis

by

SAITEJA DAMERA

Submitted to the Office of Graduate and Professional Studies of
Texas A&M University
in partial fulfillment of the requirements for the degree of

MASTER OF SCIENCE

Chair of Committee,	Aydin I. Karsilayan
Co-Chair of Committee,	Jose Silva-Martinez
Committee Members,	Peng Li
	Rainer J. Fink
Head of Department,	Miroslav M. Begovic

August 2015

Major Subject: Electrical Engineering

ABSTRACT

A new design technique for minimally invasive all-pole analog lowpass filters is introduced and the concept of minimally invasive filtering has been generalized for higher orders both in voltage-mode and current-mode operations. The proposed fully differential solution has minimal impact on the in-band signal in terms of added noise and nonlinearity, whereas it has comparable performance for out-of-band signals using smaller number of active devices.

Extending the concept of current-mode minimally invasive filters, a novel baseband circuit with third order filtering has been designed, which has comparable linearity and noise with approximately half the power consumption when compared to the conventional solution. The proposed baseband circuit has a bandwidth of $10MHz$, achieves $44dB$ rejection at $50MHz$ ($40dB$ in post-layout simulations), low broad-band input impedance of 10.16Ω with a comparable noise and linearity at a lower power consumption when compared to a third order conventional circuit. The circuit has been designed in TSMC $130nm$ technology and is integrated with a broad-band receiver front-end including an LNA and a mixer.

DEDICATION

To my wonderful parents and my loving brother

ACKNOWLEDGEMENTS

I would like to thank the people who made this research project and thesis possible. First, I would like to express many thanks to my advisor Dr. Aydin Karsilayan, who has been constantly motivating me in my research and has been a source of inspiration for me. I would like to thank me for his excellent ideas and for being patient with me throughout my research phase providing me guidance and strong support in my endeavors.

I am also grateful to Dr. Jose Silva-Martinez for serving on my committee as well as for the technical knowledge he imparted to me in his classes and in our meetings. I would like to thank him for being a critical judge and at the same time very encouraging in any of the ideas I was working on.

Special gratitude goes to Dr. Peng Li and Dr. Rainer J. Fink for taking time out of their busy schedules to serve on my committee. My peers in the Analog and Mixed Signal program deserve thanks for their helpful advice and encouragement. Specifically, I would like to thank Arun Venkatesh Alapappan for his suggestions and for his support in many of the courses that I have taken along with him.

I am deeply indebted to my friends and family for all their support throughout this project. Great appreciation goes to my parents for their belief and trust me and for being a constant emotional support in all my endeavors. I have been inspired, motivated and had the self belief to succeed in this work because of my mother and father, to whom I am deeply indebted to and thankful for. Also, I am extremely thankful towards my special friend, Carley, who has been a strong source of support and encouragement althrough this journey.

TABLE OF CONTENTS

Page

LIST OF FIGURES

Page

LIST OF TABLES

Page

CHAPTER I

INTRODUCTION

1.1 Overview

Analog filters are one of the key components of signal processing systems. Although digital implementation of filters is preferred whenever possible, communication systems usually require analog filters for anti-aliasing and blocker rejection. Rejecting out-of-band blocker signals in the vicinity of filter's cut-off frequency has become very crucial because the harmonic mixing of blockers that can corrupt the in-band signals drastically. For example, wireless communication devices for mobile-TV applications require strong blocker rejection to relax the dynamic range of the blocks, which follow the filter in the receiver [1]. Therefore, providing higher order rejection to blockers with minimum additional circuitry without degrading linearity and noise is crucial.

In this work, the concept of minimally invasive analog filtering topology, which was introduced in [2], has been extended and generalized to higher orders. The design considerations for third and fifth order Butterworth lowpass filters in voltage domain have been discussed [3], and the linearity and noise parameters were compared with Tow-Thomas filter counterparts. Extending the idea, a current-mode version of minimally invasive filter topology has been used in a broad-band receiver in which baseband filtering after the mixer is implemented in current-mode, eliminating the need for current-to-voltage (I-to-V) conversion. By using a minimally invasive filter in baseband portion, a new baseband circuit has been designed, which provides higher order filtering when compared to the conventional first order TIA solution and a comparable linearity and noise at half the power consumption.

1.2 Organization

This chapter starts the discussion with the concept of minimally invasiveness in filters and its theory and then it proceeds with the implementation of higher order minimally invasive filters and their comparison with conventional Tow-Thomas counterparts in the second chapter. The third chapter discusses the implementation of a baseband circuit based on a current-mode minimally invasive topology, which establishes the advantages of minimally invasive filters at a system level.

1.3 Concept of minimally invasive filter topology

The main idea behind minimally invasive filter topology is to embed the filter in the signal chain in such a way that it provides minimum disturbance to the signal when it is in-band and filtering off the signal when it is out of band. Embedding the filter function into the existing analog front-end not only provides reduced overhead [4], but also allows minimal impact of the added filter on the in-band signals. However, conventional filter topologies strive to achieve a minimal noise and good linearity at a cost of increased area and power consumption [5-14]. Therefore synthesizing a minimally invasive filter topology provides a new way of obtaining minimum noise and maximum linearity.

The design of a minimally invasive filter involves the synthesis of a frequency dependent impedance, which acts as a low-impedance path to ground for out-of-band signals, whereas it becomes transparent for in-band signals. Frequency dependent negative resistors (FDNR) were originally introduced in early 1970s, and used in designing higher order filter topologies [15-21]. Though the filter implementations based on FDNRs offered advantages in single-ended mode, differential implementations faced several drawbacks. Also, in most of the desired low-pass realizations, the number of op-amps used to realize an FDNR based filter was much higher than the number of op-amps used in an integrator based conventional filter counterpart. More recently in [22], an FDNR was used to provide noise shaping techniques to shift the noise out of the passband of the filter, however at the expense of increase in power consumption.

In this work, the second order minimally invasive filter topology introduced in [2], which is a frequency dependent resistor based filter implementation, has been extended to higher orders. The following sub-sections describe the theory of voltage and current-mode versions of minimally invasive filters with specific examples.

1.3.1 Voltage-mode minimally invasive filters

Figure 1 shows the general block diagram of a voltage-mode minimally invasive filter, where Z_x is the impedance synthesized to provide the desired transfer function, and the op-amp with the feedback resistor represents the input stage of the next block such as a continuous-time Σ-Δ ADC. The implementation of the filter in [2] was only second order, as shown in Fig. 2, to limit the additional overhead. The input voltage signal encounters a resistor divider with a frequency dependent impedance Z_x. When the signal is in-band, Z_x is open and the input voltage signal reaches the output with minimal distortion. As the input signal's frequency increases and goes above the cut-off frequency for the filter, Z_x starts sinking the current, which attenuates the current on the resistor R_i, attenuating the output voltage V_0.

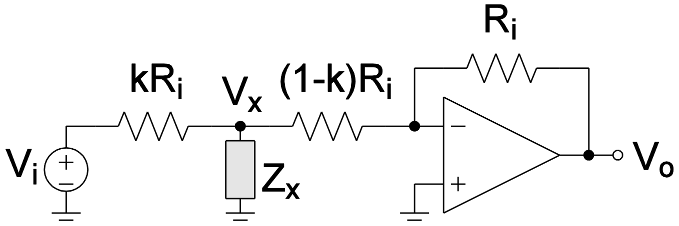

Fig. 1. Block diagram of a voltage-mode minimally invasive filter

From Fig. 1, transfer functions from V_i to V_x and V_0 can be obtained as

$$\frac{V_x}{V_i} = \frac{Z_x(1-k)}{(1-k)kR_i + Z_x} \tag{1.1}$$

$$\frac{V_0}{V_i} = \frac{Z_x}{(1-k)kR_i + Z_x} \tag{1.2}$$

1.3.1.1 Second order voltage-mode filter topology

In Fig. 2, which shows a voltage-mode second order filter, Z_x is composed of a differentiator (op-amp, R_1 and C_1) with a feedback capacitor (C_f), forming a capacitance multiplier with the frequency dependent gain of the differentiator. At low frequencies, Z_x is simply the parallel combination of C_f and C_1. At higher frequencies, C_f is multiplied by the increasing gain of the differentiator, decreasing the impedance Z_x. The resistor R_i is divided using the ratio of $k: 1-k$ to attenuate the signal at the node V_x, where the value of k was 0.5 in [2].

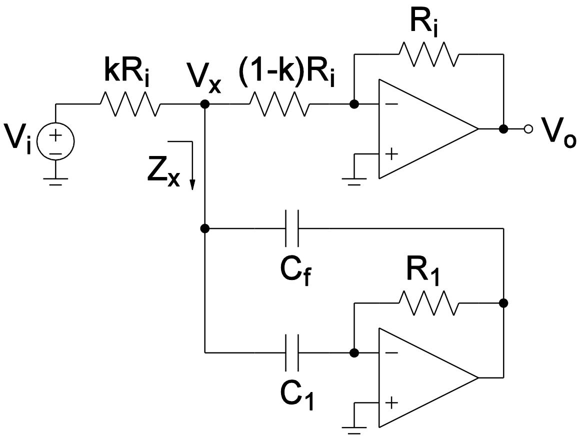

Fig. 2. Second order voltage-mode filter

For higher order filters, increasing the value of k helps in avoiding the saturation of internal nodes in the implementation of Z_x. From (1.1) and (1.2), we note that by synthesizing appropriate Z_x, the desired all-pole filter can be designed easily. The synthesized impedance according to the Fig. 2 is given by:

$$Z_x = \frac{\frac{1}{R_1 C_1 C_f}}{s^2 + \frac{C_1 + C_f}{R_1 C_1 C_f} s} \tag{1.3}$$

For example, if a second order Butterworth filter is required to be designed, we can equate the generalized voltage transfer equation for the minimally invasive filter in (1.1) with the desired Butterworth second order equation (with a gain of 0.5) as:

$$\frac{V_x}{V_i} = \frac{Z_x(1-k)}{(1-k)kR_i + Z_x} = \frac{0.5\omega_0^2}{s^2 + \sqrt{2}\omega_0 s + \omega_0^2} \tag{1.4}$$

Therefore we obtain the required impedance Z_x as:

$$Z_x = \frac{0.5\omega_0^2 R_i}{s^2 + \sqrt{2}\omega_0 s} \tag{1.5}$$

Comparing (1.3) with (1.5) we get the design requirements in terms of R and C components for the filter as:

$$\omega_0 = \sqrt{\frac{2}{R_i R_1 C_1 C_f}} \tag{1.6}$$

$$\frac{C_1 + C_f}{R_1 C_1 C_f} = \sqrt{2}\omega_0 \tag{1.7}$$

Simplifying above conditions for the case of $C_1 = C_f = C \; and \; R_1 = R_i = R$ we get,

$$\omega_0 = \frac{\sqrt{2}}{RC} \tag{1.8}$$

Considering the non-ideal case of a finite gain OTA with a specific transconductance g_m and an output impedance R_{out}, we can derive Z_x for the minimally invasive filter as follows:

$$Z_x = \frac{\frac{1}{C_f(1 + g_m R_{out})}\left(s + \frac{(1 + g_m R_{out})}{RC_1}\right)}{s^2 + \frac{C_1 + C_f}{RC_1 C_f}s} \tag{1.9}$$

We can see that the finite gain of the OTA creates a left half plane zero in the Z_x equation, which is given by:

$$\omega_Z = -\frac{(1 + g_m R_{out})}{RC_1} \tag{1.10}$$

We can control this zero by appropriately choosing a specific value of gain, R or C_1.

The elements $kR_{i,}$ $(1-k)R_i$, R_1 and the op-amp are the only contributors for noise in this filter. The noise due to kR_i and $(1-k)R_i$ are directly referred to the input, which is already budgeted in the system noise considerations since this resistance is part of signal chain as the input resistor for the summing amplifier. If the noise of resistor R_1 is denoted as V_{n,R_1}, then the noise transfer function referred to the node V_x is written as:

$$\frac{V_x}{V_{n,R_1}} = \frac{1}{R_1 C_1} \frac{s}{s^2 + \sqrt{2}\omega_0 s + \omega_0^2} \tag{1.11}$$

where $V_{n,R_1} = \sqrt{4kTR_1}$. Similarly, if the input-referred noise of the op-amp is denoted as $V_{n,opamp}$, then the noise transfer function referred to the node V_x is written as:

$$\frac{V_x}{V_{n,opamp}} = \frac{s\left(s + \frac{C_1 + C_f}{R_1 C_1 C_f}\right)}{s^2 + \sqrt{2}\omega_0 s + \omega_0^2} \tag{1.12}$$

From the above equations we notice that NTF due to noise of the resistor $R_1$and op-amp are band-pass and high-pass shaped, respectively, which have minimal contribution to the in-band noise as are shown in Fig. 3 along with the frequency response of the filter.

The major limitation for a voltage-mode minimally invasive filter is due to the need for splitting the input resistor R_i to insert the impedance Z_x. The R and C components are constrained because splitting R_i makes the competing passive resistance $(1-k)R_i$ inherently smaller, therefore designing Z_x to be much smaller than $(1-k)R_i$ at high frequencies becomes challenging. This could be alleviated by increasing the value of R_i, but that would increase the noise of the filter. Since R_i is essentially part of a next stage ADC, it is not always possible to increase its value. Also, since the input is voltage, we have to make sure that the op-amp output node V_{o1} does not become saturated. The following sub-section talks about current-mode version of the minimally invasive filter, which alleviates most of the problems mentioned here.

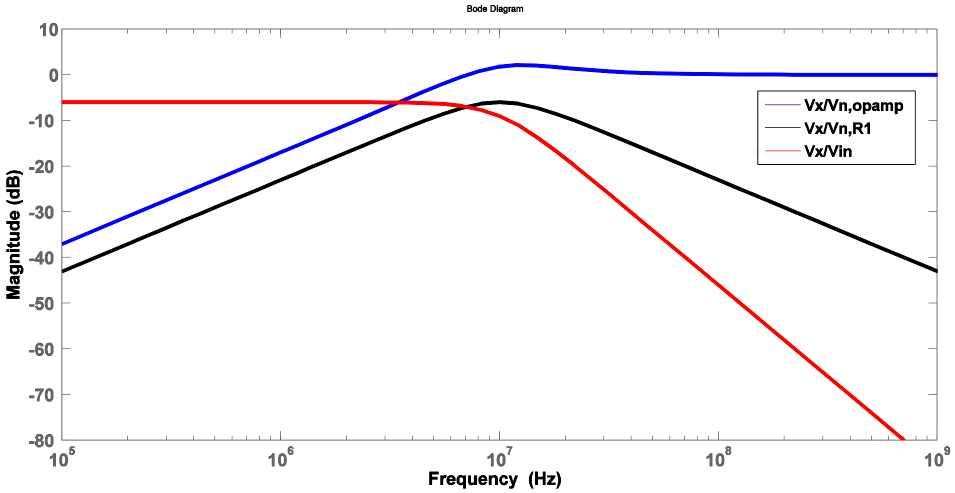

Fig. 3 Transfer functions for the second order voltage-mode filter

1.3.2 Current-mode minimally invasive filter

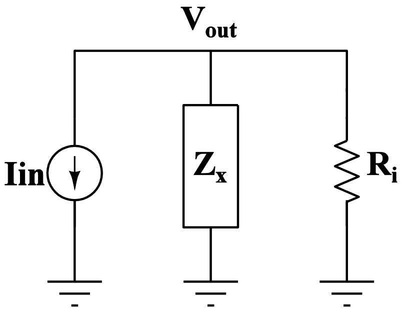

Fig. 4. Block diagram of a current-mode minimally invasive filter

The concept behind the current-mode minimally invasive filter is similar to its voltage-mode counterpart. Figure 4 shows the block diagram of the minimally invasive current-mode filter. The input current encounters a parallel combination of a passive resistor R_i and a frequency dependent impedance Z_x. When the signal is in-band, Z_x is much greater than R_i and almost the entire input current sinks into R_i, providing the required transimpedance gain. As the input signal's frequency increases and beyond the cut-off frequency for the filter, Z_x starts sinking the current, which attenuates the current on the resistor R_i, reducing the overall transimpedance gain. The transimpedance equation from input current to output voltage is given by:

$$\frac{V_{out}}{I_{in}} = \frac{R_i Z_x}{R_i + Z_x} \tag{1.13}$$

Similar to the voltage-mode filter, (1.13) is compared with the required Butterworth function to obtain the desired Z_x. The general design procedure is explained using a second order topology in the following section.

1.3.2.1 Second order current-mode filter topology

Figure 5 shows the current-mode version of the second order minimally invasive filter. The impedance Z_x is same as the impedance of the voltage-mode counterpart, as calculated in (1.3). To implement a second order Butterworth filter, we can equate the generalized transimpedance transfer equation in (1.13) with the desired Butterworth second order equation as shown:

$$\frac{V_{out}}{I_{in}} = \frac{R_i Z_x}{R_i + Z_x} = \frac{\omega_0^2 R_i}{s^2 + \sqrt{2}\omega_0 s + \omega_0^2} \tag{1.14}$$

Therefore we obtain the required impedance Z_x as:

$$Z_x = \frac{\omega_0^2 \, R_i}{s^2 + \sqrt{2}\omega_0 s} \tag{1.15}$$

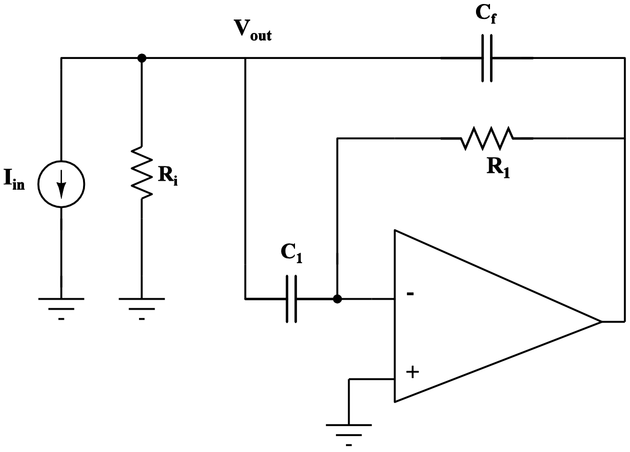

Fig. 5. Second order current-mode filter

Comparing (1.3) with (1.15) we get the design requirements in terms of R and C components for the filter as:

$$\omega_0 = \sqrt{\frac{1}{R_i R_1 C_1 C_f}} \tag{1.16}$$

$$\frac{C_1 + C_f}{R_1 C_1 C_f} = \sqrt{2}\omega_0 \tag{1.17}$$

Simplifying above conditions for the case of $C_f = aC_1$ we get,

$$R_1 = \frac{(a+1)^2}{2a} R_i \tag{1.18}$$

From the above equations we can calculate the value of R and C components required for the filter for a desired cut-off frequency and input resistance R_i. The major advantage of having a current-mode filter is that the resistor R_i is not split and therefore R_1 can be high enough to relax the burden on the op-amp used in the filter. Also, the noise transfer functions due to the op-amp noise $V_{n,opamp}$ and due to the resistor R_1 follow the same expressions as derived in (1.12) and (1.11).

CHAPTER II

DESIGN OF HIGHER ORDER VOLTAGE-MODE MINIMALLY INVASIVE LOWPASS FILTERS*

2.1 Introduction

In this chapter, higher order implementation of voltage-mode minimally invasive filters is presented, where impedance Z_x is modified to generate higher order filters, while retaining the key advantages of minimally invasive topology. Design procedure and simulation results are provided in the following sections.

2.2 Synthesis of higher order all-pole filters

2.2.1 General procedure

Higher order functions require synthesizing higher order Z_x for the desired filter approximation. Since the impedance Z_x needs to be large at low frequencies to allow the input signal to pass through the signal path, $Z_x$needs to be capacitive. We can see that in the realized impedance in Fig. 6 and Fig. 7, Z_x is predominantly capacitive. As the input signal frequency increases, Z_x starts sinking in current from the signal path, attenuating the input signal. Table I shows the impedance expressions for various filter orders.

---

[*] Parts of the data reported in this chapter is reprinted with permission from “Design of Minimally Invasive All Pole Analog Lowpass filters” by Saiteja Damera, Aydin I. Karsilayan and Jose Silva Martinez, 2014. IEEE International Midwest Symposium on Circuits and Systems (MWSCAS), Copyright [2014] by IEEE.

Table I. Synthesized impedances for various filter orders

Filter Order	**Z_X**
2nd	$\dfrac{\frac{1}{R_1C_1C_f}}{s^2+\frac{C_1+C_f}{R_1C_1C_f}s}$
3rd	$\dfrac{\frac{1}{R_1R_2C_1C_2C_f}}{s^2+\frac{R_1+R_2}{R_1R_2C_2}s^2+\frac{C_1+C_f}{R_1R_2C_1C_2C_f}s}$
4th	$\dfrac{\frac{1}{a_0b_1C_f}}{s^4+\frac{b_2}{b_1}s^3+\left(\frac{b_3}{b_1}+\frac{R_xC_xC_Z}{a_0b_1C_f}\right)s^2+\left(\frac{C_0+C_f+C_x+C_z}{s_0b_1C_f}\right)s}$ Where $a_0=R_3C_0, b_1=R_1R_2C_1C_2, b_2=R_1C_1\left(1+\frac{R_2}{R_3}\right)+(R_1+R_2)C_2, b_3=1+\left(\frac{R_1+R_2}{R_3}\right)$

The following sections show the design procedure of implementing a third order and a fifth order Butterworth filter based on the above mentioned idea.

2.2.2 Third order lowpass filter

Figure 6 shows the third-order minimally invasive all-pole lowpass filter. The impedance Z_x is derived assuming an ideal op-amp, and is shown in table I. By equating the third order Butterworth lowpass transfer function to (1.2), we obtain

$$\frac{V_0}{V_i}=\frac{Z_x(1-k)}{(1-k)kR_i+Z_x}=\frac{0.5\omega_0^3}{s^3+2\omega_0s^2+2\omega_0^2s+\omega_0^3} \tag{2.1}$$

$$Z_x=\frac{\mathrm{k}(1-\mathrm{k})\omega_0^3R_i}{s^3+2\omega_0s^2+2\omega_0^2s} \tag{2.2}$$

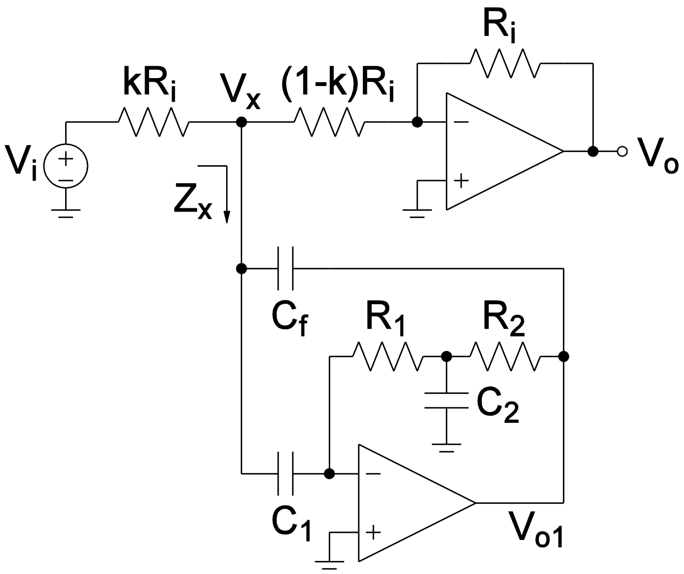

Fig. 6. Third order minimally invasive filter topology

Combining (2.2) with the 3rd order Z_x function in table I and assuming that $R_1 = R_2 = R$, we can calculate the required component values as:

$$\omega_0 = \frac{1}{RC_2} \tag{2.3}$$

$$R = \frac{(1-k)kR_iC_1C_f}{C_2^2} \tag{2.4}$$

$$\frac{C_1 + C_f}{C_1C_f} = \frac{2}{C_2} \tag{2.5}$$

The transfer function from V_i to the op-amp output node V_{o1} is given by

$$\frac{V_{o1}}{V_i} = \frac{(1-\mathrm{k})\omega_0^3(sRC_1)(2+sRC_2)}{s^3 + 2\omega_0 s^2 + 2\omega_0^2 s + \omega_0^3} \tag{2.6}$$

At ω_0, (2.6) is simplified as

$$\left.\frac{V_{o1}}{V_{in}}\right|_{\omega=\omega_0} = \sqrt{\frac{5}{2}}(1-k)\frac{C_1}{C_2} \tag{2.7}$$

If we assume $C_1 = a_1 C_2$ and $C_f = a_2 C_2$ where a_1 and a_2 are two non-zero positive real variables then (2.5) becomes,

$$a_1 + a_2 = 2a_1 a_2 \tag{2.8}$$

then (2.4) is simplified as

$$R = (1-k)kR_i a_1 a_2 \tag{2.9}$$

and (2.7) is simplified as

$$\left.\frac{V_{o1}}{V_{in}}\right|_{\omega=\omega_0} = \sqrt{\frac{5}{2}}(1-k)a_1 \tag{2.10}$$

The value of RC_2 is determined by the desired ω_0 value. The k value was chosen as 0.5 and the values of $a_1(=0.5)$ and $a_2(=20)$ are chosen such that there is no peaking at the op-amp output node V_{o1}. The values of components are obtained as $R_i = 800\ \Omega, R = 2.05\ k\Omega, C_2 = 15.5\ pF, C_1 = 7.9\ pF\ and\ C_f = 310\ pF$. These values are calculated for a ω_{3dB} cutoff frequency of 5 MHz.

2.2.3 Fifth order lowpass filter

Fifth order Butterworth filter is implemented by using a 4th order Z_x function and replacing the summing amplifier with an integrator to provide the additional real pole as shown in Fig. 7.

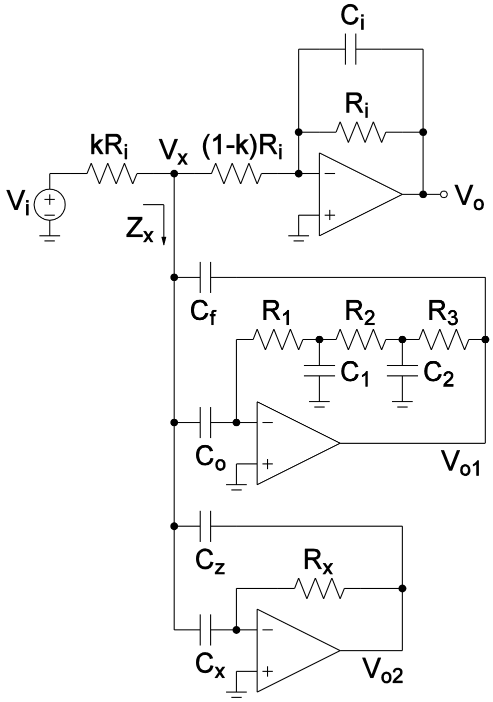

Fig. 7. Fifth order minimally invasive filter topology

The fifth order Butterworth lowpass function is factorized into fourth order and first order sections as

$$\frac{V_0}{V_i} = \frac{0.5\omega_0^5}{s^5 + 3.236\omega_0 s^4 + 5.235\omega_0^2 s^3 + 5.235\omega_0^3 s^2 + 3.236\omega_0^4 s + \omega_0^5}$$
$$= \left(\frac{0.5\omega_0^4}{s^4 + 2.236\omega_0 s^2 + 3\omega_0^2 s + 2.236\omega_0^3 s + \omega_0^4}\right)\left(\frac{\omega_0}{s + \omega_0}\right) \quad (2.11)$$

The fourth order lowpass equation from (2.11) is compared with (1.1) to obtain,

$$\frac{V_0}{V_i} = \frac{Z_x(1-k)}{(1-k)kR_i + Z_x} = \frac{0.5\omega_0^4}{s^4 + 2.236\omega_0 s^2 + 3\omega_0^2 s + 2.236\omega_0^3 s + \omega_0^4} \quad (2.12)$$

$$Z_x = \frac{\mathrm{k}(1-\mathrm{k})\omega_0^4 R_i}{s^4 + 2.236\omega_0 s^3 + 3\omega_0^2 s^2 + 2.236\omega_0^3 s} \tag{2.13}$$

Combining (2.13) with the 4th order Z_x function in table I, we can calculate the required components values. Assuming that $R_1 = R_2 = R_3 = R$ and $C_1 = C_2 = C$, the design equations are obtained as:

$$\omega_0 = \frac{1.788}{RC_2} \tag{2.14}$$

$$R = \frac{10.22(1-k)kR_iC_0C_f}{C^2} \tag{2.15}$$

$$\frac{C_0 + C_f + C_x + C_z}{C_0C_f} = \frac{12.78}{C} \tag{2.16}$$

$$R_z = \frac{6.59RC_0C_f}{C_xC_z} \tag{2.17}$$

To check for possible saturation caused by peaking at op-amp outputs, we derive the transfer functions from V_i to op-amp output nodes V_{o1} and V_{o2} as

$$\frac{V_{o1}}{V_i} = \frac{(1-\mathrm{k})\omega_0^4(sRC_0)((2+RsC)^2-1)}{s^4 + 2.236\omega_0 s^3 + 3\omega_0^2 s^2 + 2.236\omega_0^3 s + \omega_o^4} \tag{2.18}$$

$$\frac{V_{o2}}{V_i} = \frac{(1-\mathrm{k})\omega_0^4(sR_xC_x)}{s^4 + 2.236\omega_0 s^3 + 3\omega_0^2 s^2 + 2.236\omega_0^3 s + \omega_o^4} \tag{2.19}$$

At ω_0, the above equations become

$$\left.\frac{V_{o1}}{V_{in}}\right|_{\omega=\omega_0} = 12.81(1-k)\frac{C_0}{C} \tag{2.20}$$

$$\left.\frac{V_{o1}}{V_{in}}\right|_{\omega=\omega_0} = 1.788(1-k)\frac{R_Z}{R}\frac{C_x}{C} \tag{2.21}$$

If we assume $C_0 = a_1C, C_f = a_2C, C_x = a_3C\ and\ C_z = a_4C$ where a_1, a_2, a_3, a_4 are four non-zero positive real variables then the (2.16) becomes,

$$a_1 + a_2 + a_3 + a_4 = 12.78a_1a_2 \tag{2.22}$$

(2.15), (2.17), (2.18) and (2.19) are simplified as

$$R = 10.22(1-k)kR_ia_1a_2 \tag{2.23}$$

$$R_z = 6.59R\frac{a_1a_2}{a_3a_4} \tag{2.24}$$

$$\left.\frac{V_{o1}}{V_{in}}\right|_{\omega=\omega_0} = 12.81(1-k)a_1 \tag{2.25}$$

$$\left.\frac{V_{o1}}{V_{in}}\right|_{\omega=\omega_0} = 8.48(1-k)\frac{a_1a_2}{a_4} \tag{2.26}$$

From (2.25) and (2.26), C_0, C_f, C_x and C_z values are chosen such that there is no peaking at the op-amp output nodes V_{o1} and V_{02}. The values of components are obtained as $R_i = 800\ \Omega, k = 0.76, R = 728\ \Omega, C = 78.2\ pF, C_0 = 12.7\ pF, C_f = C_z = 234\ pF, R_x = 7.8\ k\Omega\ and\ C_x = 7.8\ pF$. These values are calculated for a ω_{3dB} cut-off frequency of

$5MHz$. Fourth order Butterworth filter can also be implemented in a similar way by changing the coefficients and re-calculating component values, with no additional pole provided by the summing amplifier.

2.2.4 Design of the op-amp

A two-stage fully differential Miller compensated op-amp with a class AB stage as shown in Fig. 8 has been designed to be used for the voltage-mode minimally invasive filter. The two-stage architecture has been chosen to achieve a moderate gain and with sufficient Miller compensation. The input stage has PMOS transistors to reduce the flicker noise component. The op-amp was designed in 180nm CMOS technology to provide $50dB$ DC gain and $260MHz$ gain-bandwidth product with a single power supply of $1.8V$. The op-amp has an input common-mode voltage level at 0.9V, which is the midpoint of the power supply to have an optimum output voltage swing.

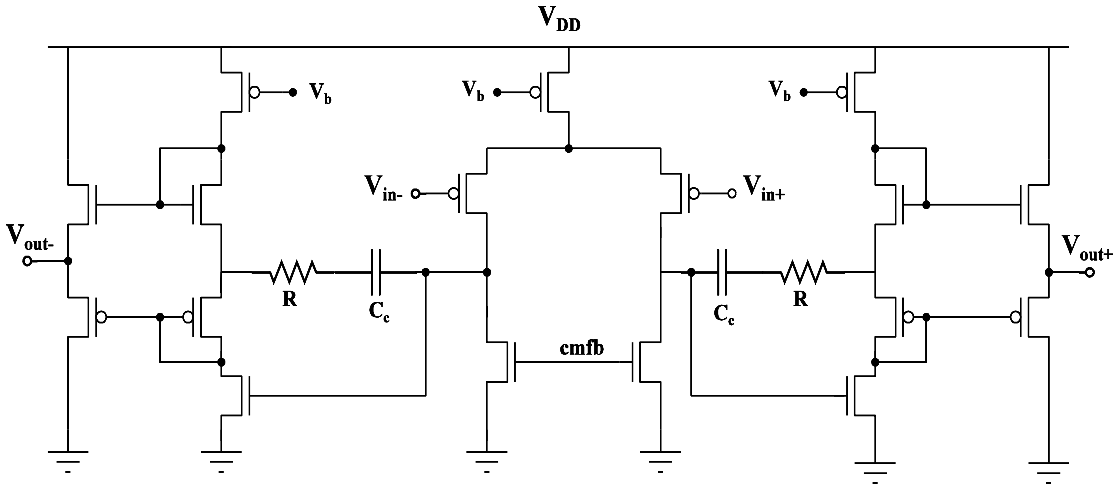

Fig. 8. Schematic of the op-amp

2.3 Simulation results

Using the designed op-amp, 3^{rd} and 5^{th} order minimally invasive filters in Figs. 6 and 7, and Tow-Thomas filters (3^{rd} order is shown in Fig. 9) have been designed. For comparison, Tow-Thomas topology was selected because it offers a fully differential implementation with better stability. The input resistor $R_i = 800\ \Omega$ was kept the same for both filter types since it is the major source of thermal noise. For the third order Tow-Thomas filter, all capacitors are equal to $40\ pF$ for a ω_{3dB} frequency of $5MHz$. Similarly, the fifth order Tow-Thomas filter has five op-amps with all the capacitor values in the fourth order section equal to $20\ pF$, while the first order integrator has a capacitance of $40\ pF$.

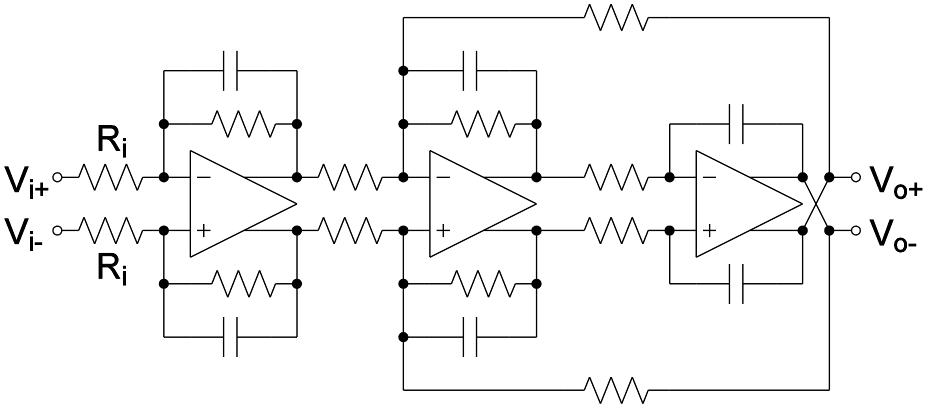

Fig. 9. Tow-Thomas third order filter

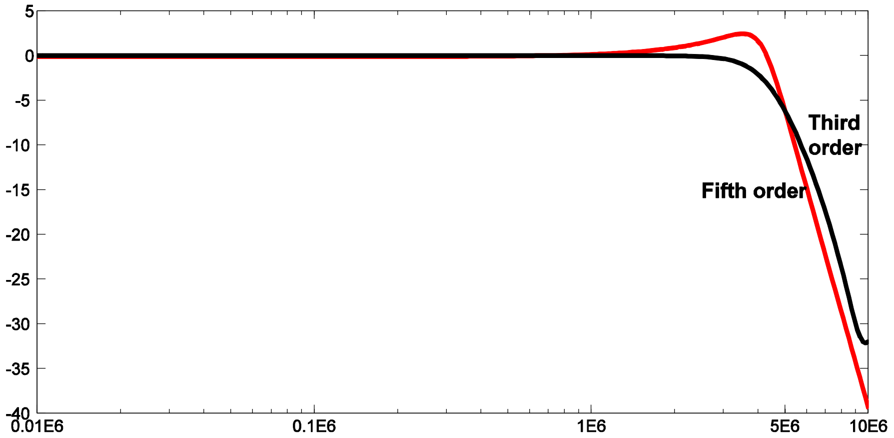

Fig. 10. Frequency response of third and fifth order minimally invasive filters

It can be seen that minimally invasive 3rd order filter requires only two op-amps including the summing amplifier, which is typically a part of the existing circuit as in the case of continuous-time Σ-Δ ADCs. Further increasing the order by two requires only one additional op-amp, whereas Tow-Thomas requires two. Figure 10 shows the frequency response of third and fifth order minimally invasive filters. For the third order case, the summing amplifier is an ideal op-amp since the filtering action is performed only by the impedance part of the filter. The results with actual op-amp as a summing amplifier have also been noted for comparison both for the third and fifth order filters since the only invasive component in this architecture is the summing amplifier, which degrades linearity. Figure 11 shows the in-band two-tone test simulation results of 3rd order minimally invasive and Tow-Thomas filters, whereas out-of-band linearity results are shown in Fig. 12.

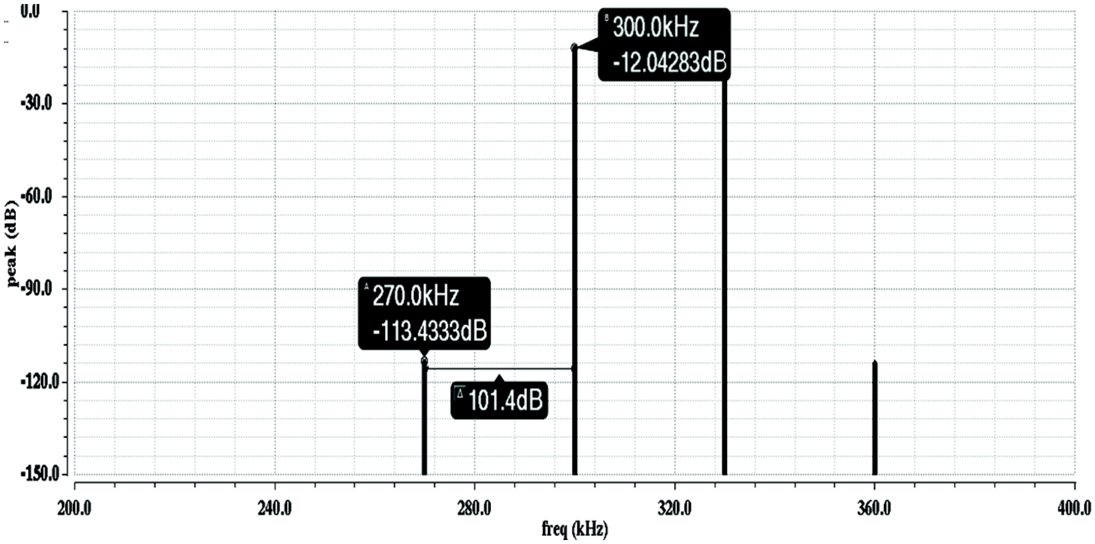

(a)

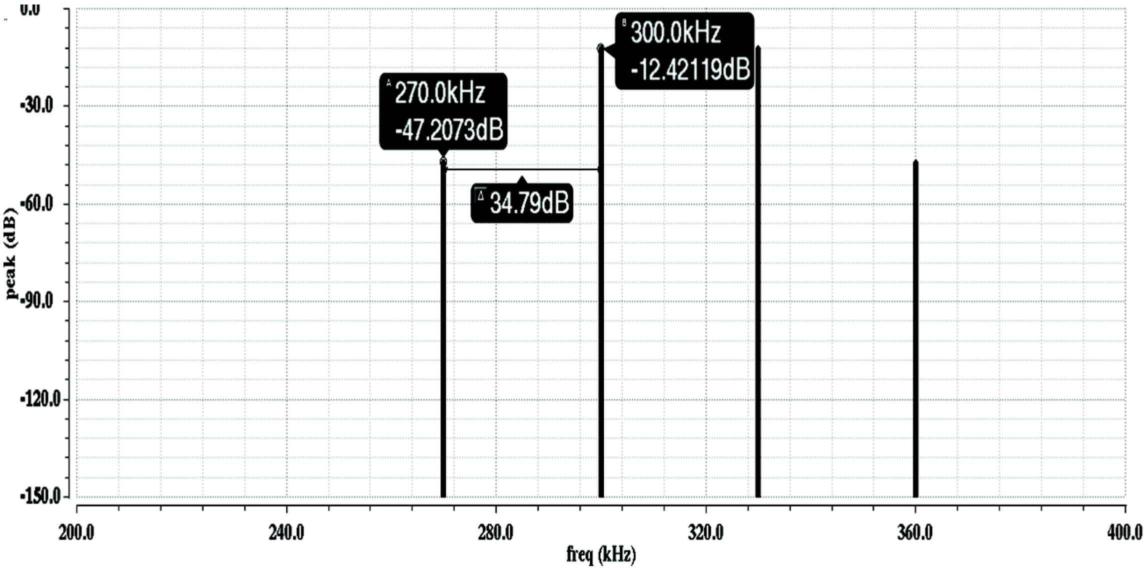

(b)

Fig. 11 In-band IM_3 plots for third order case (a) Minimally invasive filter (b) Tow-Thomas filter (with ideal summing op-amp)

Two input tones at $f_1 = 300\,KHz\ and\ f_2 = 330\,KHz$ produce in-band inter-modulated tones. For the out-of-band two-tone test, tones at $f_1 = 8.75\,MHz\ and\ f_2 =$

15 MHz are applied to the input, producing a third-order inter-modulated tone at 2.5 MHz, which falls in-band for the filter. These plots are shown in Fig. 13.

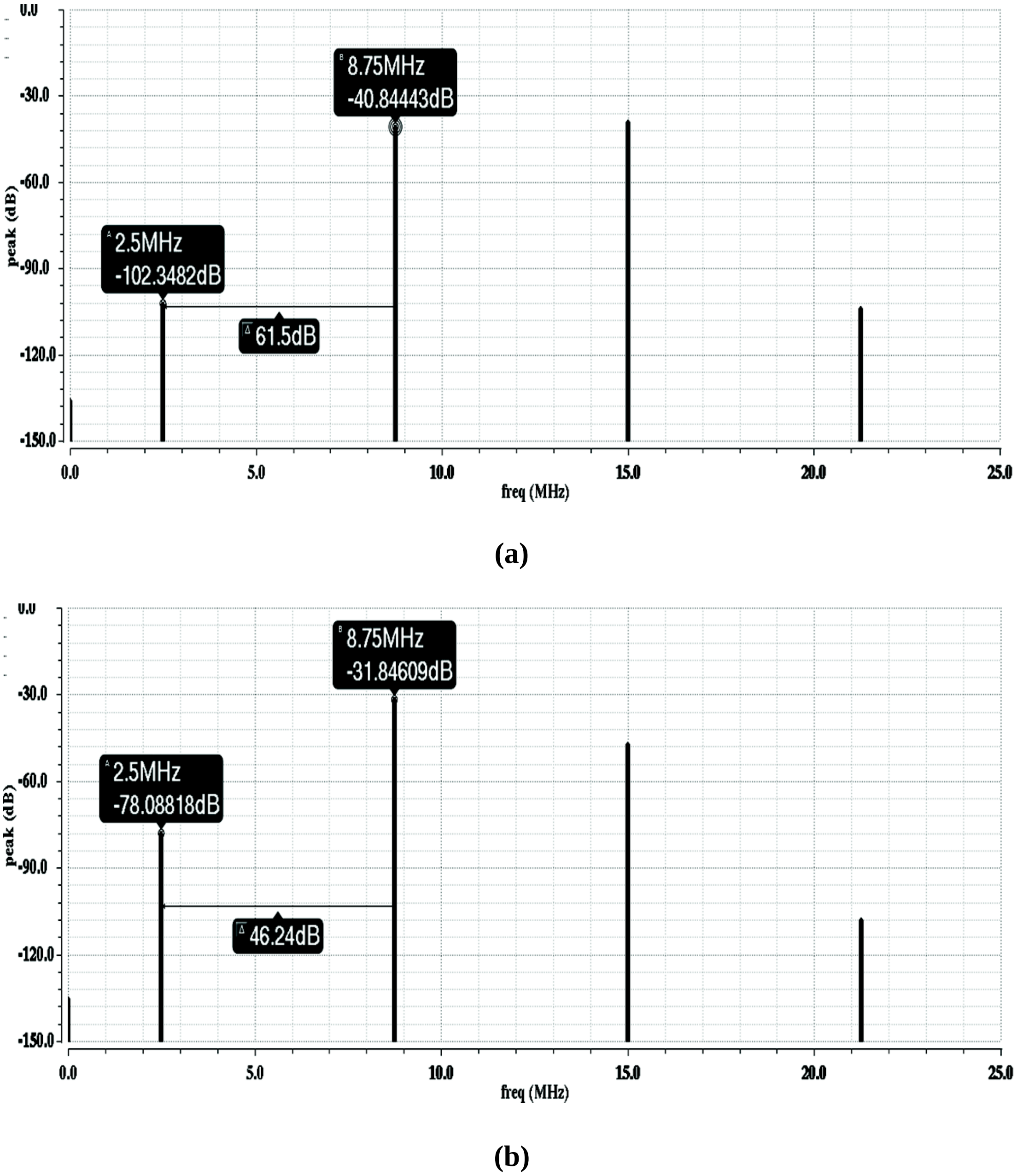

(a)

(b)

Fig. 12. Out-of-band IM_3 plots for third order case (a) Minimally invasive filter (b) Tow-Thomas filter (with ideal summing op-amp)

Figure 13 shows the in-band two-tone test simulation results of 5th order minimally invasive and Tow-Thomas filters, whereas out-of-band linearity results are shown in Fig. 14.

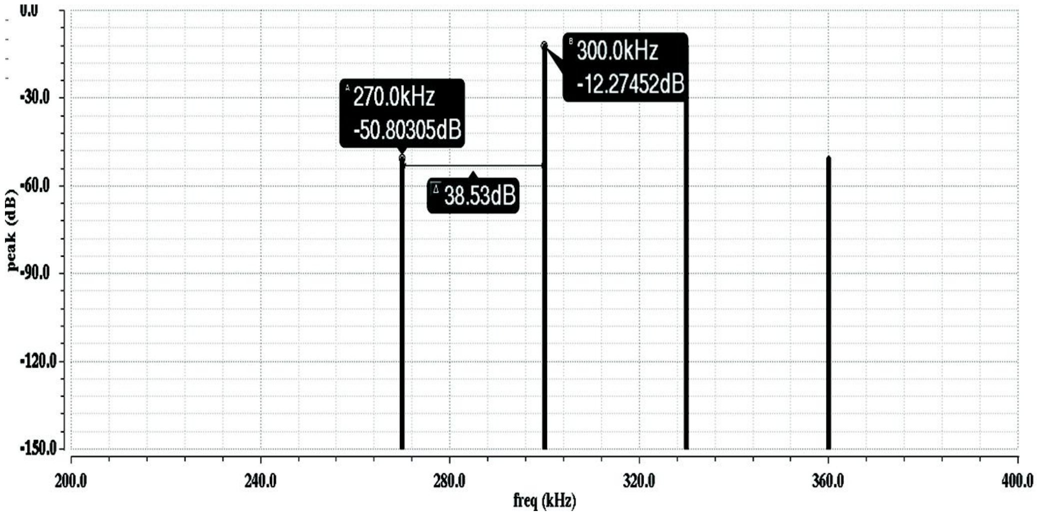

(a)

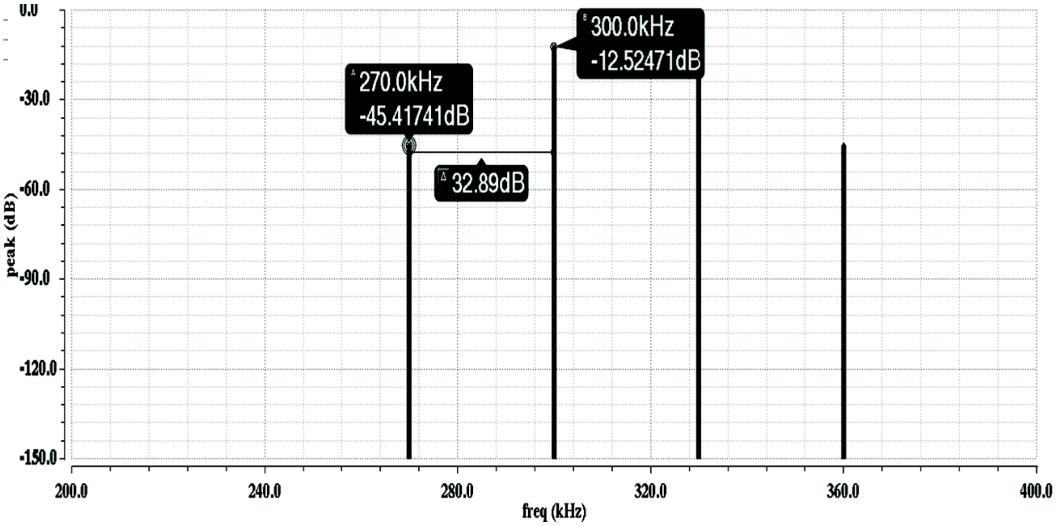

(b)

Fig. 13. In-band IM_3 plots for fifth order case (a) Minimally invasive filter (b) Tow-Thomas filter (with actual op-amp)

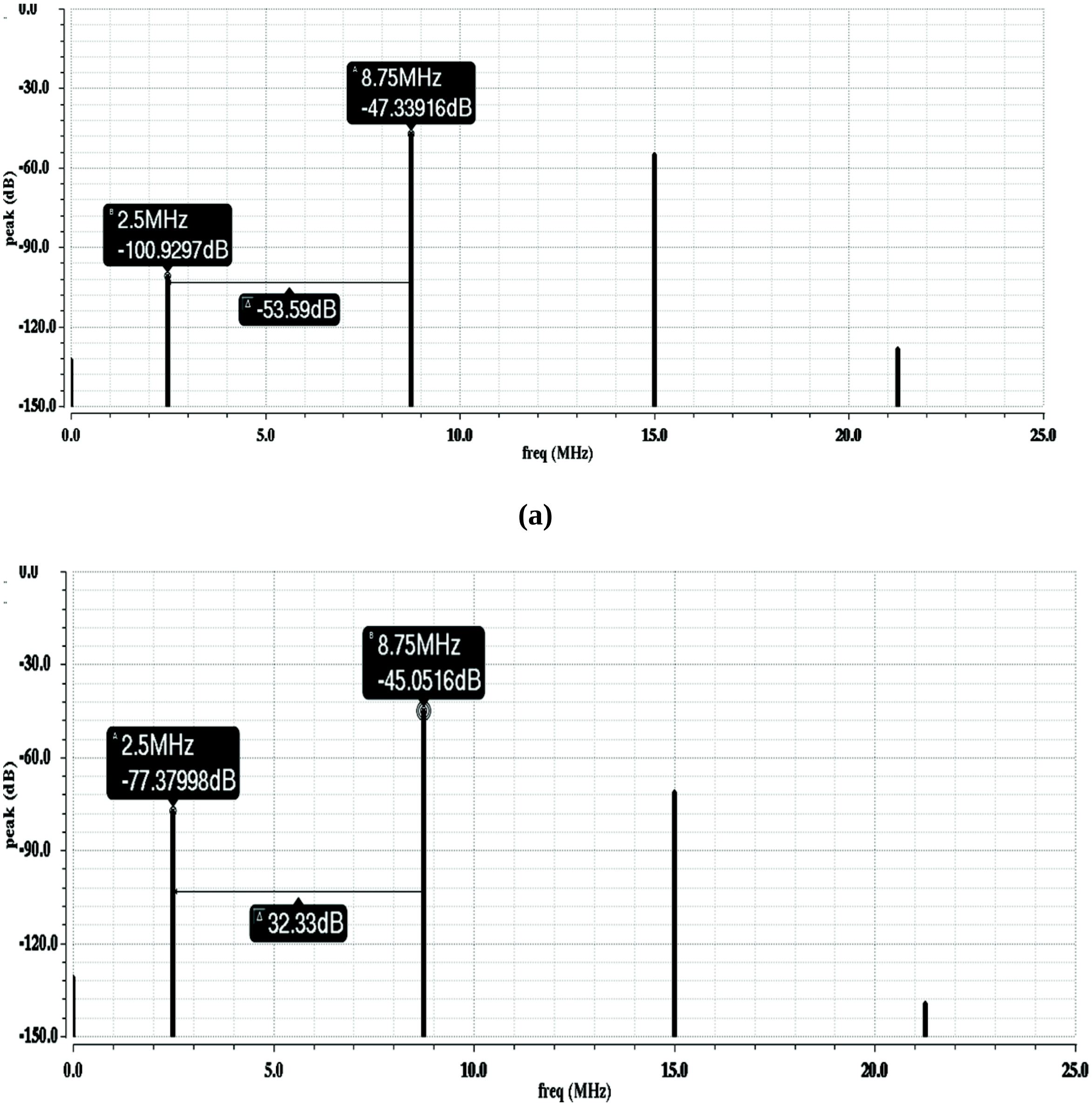

(a)

(b)

Fig. 14. Out-of-band IM_3 plots for fifth order case (a) Minimally invasive filter (b) Tow-Thomas filter (with actual op-amp)

The simulation results including input-referred noise (integrated in-band) and linearity of the 3rd and 5th order minimally invasive filters are summarized in table II along with the values for Tow-Thomas counterparts. The degradation in linearity from the case where the summing op-amp is ideal to the case where the summing op-amp is a real one is because of the fact that the summing op-amp is present in the signal path, thereby reducing its linearity even though it does not perform any filtering in case of a minimally invasive filter architecture. Generally, the summing amplifier is part of the next stage of the system, for example, it could represent an input stage of an ADC.

Table II Simulation results (a) Third order (b) Fifth order

3rd Order	Minimally Invasive		Tow-Thomas
	Summing Op-amp		
	Ideal	Actual	
In-band ID3 (dB)	101.4	38.07	34.79
Out-of-band ID3 (dB)	61.5	59.56	46.24
Total Input-referred Noise (nV)	0.785	1.515	2.880

(a)

5th Order	Minimally Invasive		Tow-Thomas
	Summing Op-amp		
	Ideal	Actual	
In-band ID3 (dB)	101.7	38.53	32.89
Out-of-band ID3 (dB)	53.79	53.68	32.33
Total Input-referred Noise (nV)	3.333	4.420	5.874

(b)

CHAPTER III

DESIGN OF A CURRENT-MODE BASEBAND CIRCUIT FOR A BROAD-BAND RECEIVER USING MINIMALLY INVASIVE FILTER TOPOLOGY

3.1 Introduction

3.1.1 Background

The ever growing demand for wireless applications and its use in portable devices has fueled the need for low power receivers with improved performance in linearity and noise. Recently, direct-conversion receivers have been used widely because of their higher level of integration and baseband flexibility. Direct conversion receivers convert radio frequency (RF) signals directly down to DC instead of an intermediate non-zero frequency (IF) as in heterodyne receivers, which eliminates the creation of image tone that interferes with the down converted signal. Also, a direct-conversion receiver topology eliminates the need for band-pass filters and it only requires lowpass filters to eliminate blockers [23].

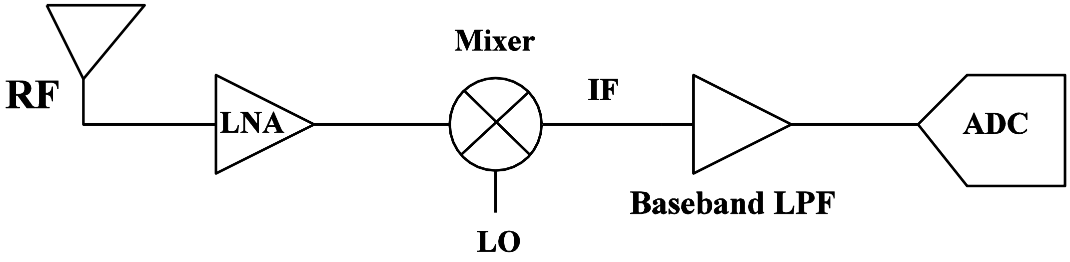

Fig. 15. Block diagram of a direct-conversion broad-band receiver

Figure 15 shows the block diagram of a direct-conversion receiver. In the first stage, the LNA presents a stable 50Ω input impedance to the RF signal while amplifying it before it is down-converted by the mixer in second stage. The mixer has a local oscillator (LO) signal, whose frequency is set equal to the RF frequency to down-convert the RF signal into DC. After the mixer, a lowpass filter is used to filter off the blockers and harmonics. Then, the signal passes through an analog-to-digital converter (ADC) for further processing in digital domain.

Noise and linearity are crucial parameters in direct-conversion receivers. Since, the down-converted signal is at very low frequencies, flicker noise becomes very important. The accuracy of the ADC improves with reduction in noise in the analog front-end. The down-conversion of the RF signal happens at the mixer, making it the most important block when it comes to flicker noise. One of the ways to reduce flicker noise in the mixer is to have less current when the mixer is switching i.e. passive mixers are preferable since they offer zero DC current compared to active mixers such as Gilbert cell mixers, which have a non-zero DC current [24]. However it has been shown in [25] that a time-varying non-zero DC current will still generate flicker noise but passive mixers show substantially lesser flicker noise compared to active mixers. Therefore, a current-mode passive mixer is generally used in direct-conversion receivers, which requires a current output low-noise transconductance amplifier (LNA) and a transimpedance lowpass filter to convert the current output of the mixer to a voltage. In this chapter, design of a current-mode receiver chain has been discussed, in which baseband filtering after the mixer is performed in current-mode, eliminating the need for I-to-V conversion before processing by the ADC.

3.1.2 Baseband TIA and its drawbacks

Conventional direct-conversion receiver has a TIA stage after the mixer, which provides current to voltage conversion for the signal while providing low input impedance for mixer output signal as shown in Fig. 16. The main purpose of the TIA is to convert small amplitude output current signals from the mixer to a large voltage and attenuate the out-of-band signals of the mixer output. Therefore a large transimpedance gain with higher order filtering is needed. In addition, the TIA needs to have a very small voltage swing at its input for large current signals from mixer. This criteria is achievable only when TIA has very low input impedance throughout a large frequency bandwidth. By having a small input impedance, the linearity of the mixer and TIA are improved drastically since the system can tolerate large amplitude current signals, without saturating the TIA input node. The TIA input is generally a differential CMOS transistor pair whose transistors operate in saturation region while the passive current mixer has transistors, which operate in triode region. The linearity of the TIA is limited by the overdrive voltage of its input transistors; while for the mixer, as long as the drain-source voltage $v_{ds}$of the transistors is small, the transistors operate in linear region and the channel resistance is given by [26]:

$$R_{on} = \left[\mu C_{0x} \frac{W}{L} \left(V_{gs} - V_{th}\right)\right]^{-1} \tag{3.1}$$

where μ is the mobility of the charge carriers, C_{ox} is the capacitance of the oxide layer, $\frac{W}{L}$ is the width over length of a transistor, V_{gs} is the gate source voltage and $V_{th}$is the threshold voltage of the transistor.

Linearization techniques such as source-degeneration can be used for the TIA input transistors, but once the V_{ds} starts increasing for mixer transistors, the linearity degrades because of the non-linear resistance of the mixer. Therefore having a low input impedance at the TIA is very important for linearity.

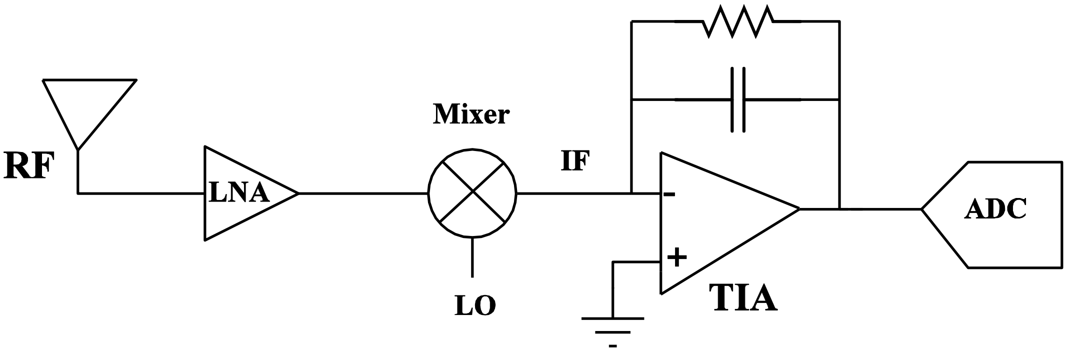

Fig. 16 Receiver with a TIA in baseband portion

3.1.3 Motivation and outline

The reference design used in this chapter is a broad-band direct-conversion receiver [27] operating from 1 GHz to 5.2 GHz. The receiver designed in [27] has a conversion gain of $22.4\, dB$ with a noise figure $(6.5\, dB - 8.3\, dB)$ at an $IIP_3 \geq -1.5\, dBm$, whose performance results are better than the receivers designed in similar operating frequencies [28-32]. It has a current-mode passive mixer followed by a transimpedance amplifier, which has a gain of $66dB$ (2kΩ). However, the TIA has only a first order roll-off after a ω_{3dB} cut-off frequency of $10MHz$, which offers only an attenuation of around $20dB$ around $100MHz$ The major goal of filtering in analog domain is to reject the interferers and reduce their power as much as possible so that the following ADC can have relaxed specifications. By reducing the interferer power levels after filtering, we can reduce the specifications of the following stage ADC. In the proposed receiver, instead of a conventional transimpedance amplifier with first order RC filtering, a cascade of a current buffer and a third order minimally invasive filter are used in the baseband portion for better linearity and lower noise and inherently higher order filtering in current-mode, while offering lower input impedance to the mixer.

3.2 Proposed architecture

In the proposed current-mode receiver architecture, two different implementations for the current buffer are investigated. As shown Fig. 17, the first implementation is based on a common-gate current buffer, which provides the interface between the mixer and the minimally invasive third order current-mode filter.

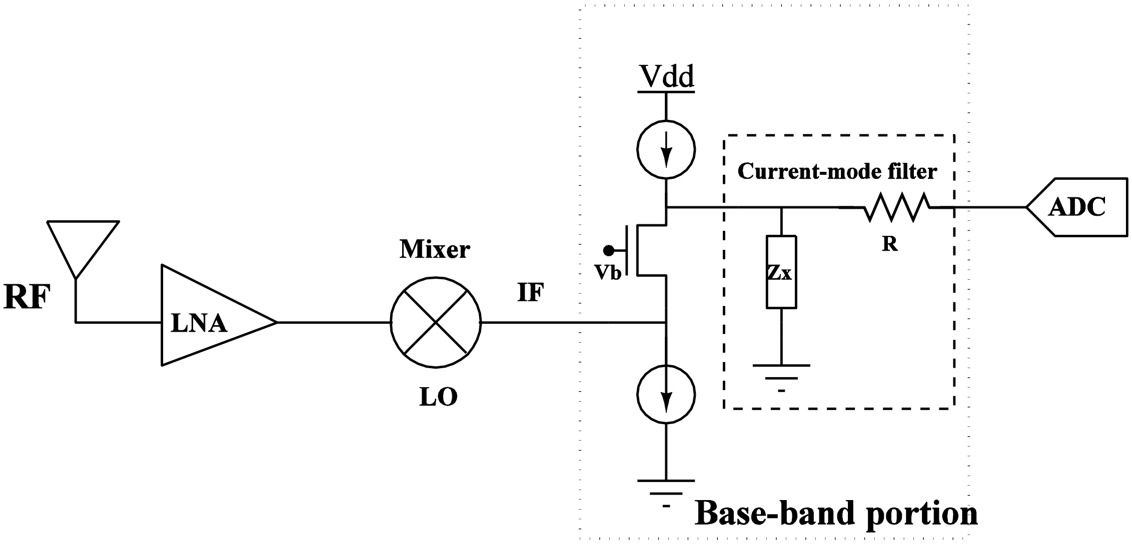

Fig. 17 Receiver block diagram with a current-mode baseband portion

The second approach, as shown in Fig. 18 is based on an op-amp in negative feedback with a common source amplifier, which provides the required low input impedance while preserving the linearity achieved through the feedback structure. The following current mirror injects the signal into the filter. The feedback architecture provides better linearity at the cost of using an additional op-amp to provide feedback, which increases power consumption.

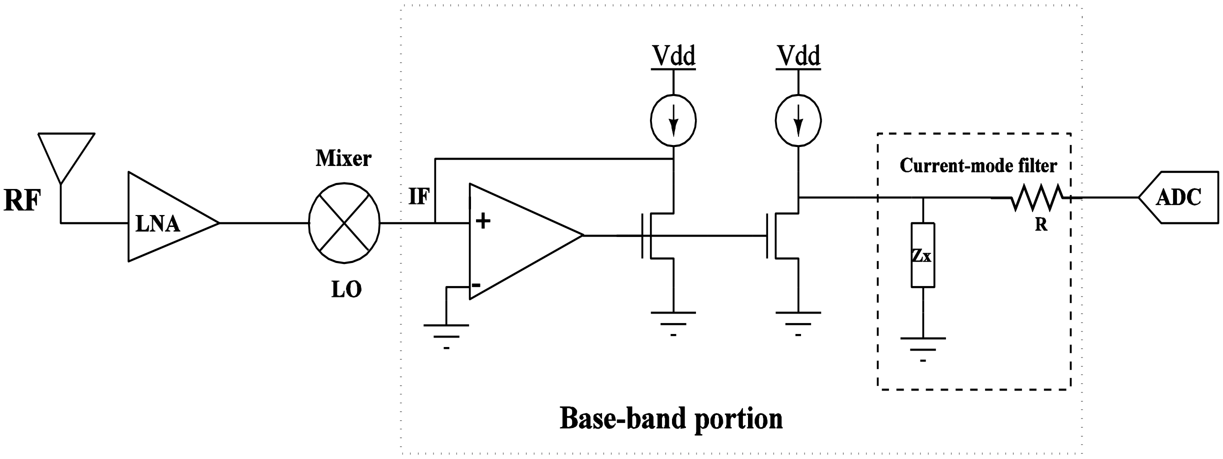

Fig. 18 Receiver block diagram with a feedback current-mode baseband portion

In both the proposed architectures, the filtered output current, is fed into the input stage of an ADC, where the resistance *R* shown in Fig. 17 and Fig. 18 is common to the filter and the input stage of the ADC.

3.3 Theoretical calculations

3.3.1 Existing TIA

The conventional solution is a transimpedance amplifier (TIA) as shown in Fig. 19. The baseband portion has a low input impedance, which is very crucial for linearity, which is given by

$$Z_{in} = \frac{Z_{TIA}}{1 + A_v} \tag{3.2}$$

where A_v is the voltage gain of the amplifier and Z_{TIA} is the feedback impedance of the TIA and is given by

$$Z_{TIA} = \frac{R}{1 + sRC} \tag{3.3}$$

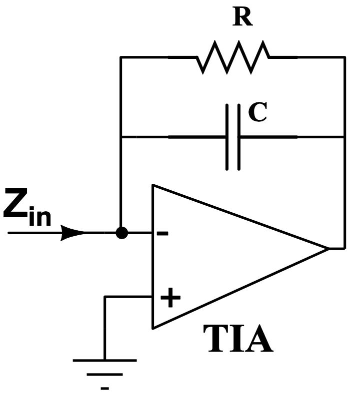

Fig. 19. Input Impedance of a TIA

The transimpedance gain is given by:

$$\frac{V_{out}}{I_{in}} = \frac{R}{1 + sRC} \tag{3.4}$$

By having a sufficiently large gain for the op-amp, TIA provides the necessary low impedance at the input of the baseband circuit, while having an input-referred current noise given by

$$I_{n,in}^2 = \frac{4kT}{R} \tag{3.5}$$

We can see that the feedback resistance noise is directly referred to input in the TIA when the op-amp is ideal, Therefore, the conventional TIA has direct trade-off between noise, the desired transimpedance gain and input impedance.

3.3.2 Common-gate current buffer

A common-gate (CG) current buffer has design trade-offs between input impedance, noise and voltage headroom [33]. Considering the circuit shown in Fig. 20, the input current directly passes to the output through the transistor M_1, which offers a low impedance. The capacitor C_{in} is added at the input to reduce the peaking of the input impedance at high frequencies. The current transfer function is given by

$$\frac{I_{out}}{I_{in}} = \frac{g_{m1}}{sC_{in} + g_{m1}} \tag{3.6}$$

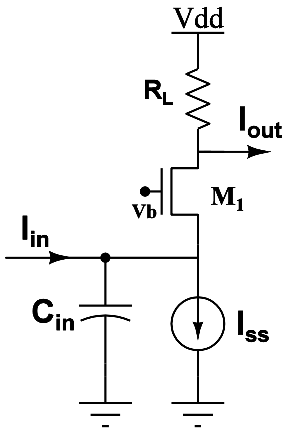

Fig. 20. Common-gate current buffer

At low frequencies, the current gain is approximately unity, whereas the input impedance and input-referred current noise can be derived as:

$$Z_{in} = \frac{1}{g_{m1}} \tag{3.7}$$

$$I_{in,in}^2 = \frac{4kT}{R_L} + I_{n,ISS}^2 \tag{3.8}$$

It is observed that the noise of tail current source I_{ss} is directly reflected at the input in (3.8). Since the transconductance has to be increased to minimize input impedance, which increases the thermal current noise of the tail current source, there is a trade-off between minimum input impedance achievable and input-referred current noise in this architecture. Therefore, a modification in the architecture is required, which boosts the g_m of the input transistor without much increase in bias current for a comparable noise performance. This is achieved in Fig. 21, where the ideal current sources have been replaced with transistors M_2, M_5 and M_6 while the transistor M_3 is used for boosting the transconductance of the input transistor M_1. The current gain from is given by

$$\frac{I_{out}}{I_{in}} = \frac{g_{m1}\left(1 + g_{m3}(g_{ds6} + g_{ds3})\right)}{\left[(g_{ds2} + sC_{in}) + g_{m1}\left(1 + g_{m3}(g_{ds6} + g_{ds3})\right)\right]} \tag{3.9}$$

From (3.9), we can see that at low frequencies, the current gain becomes approximately unity, as shown in Fig. 22.

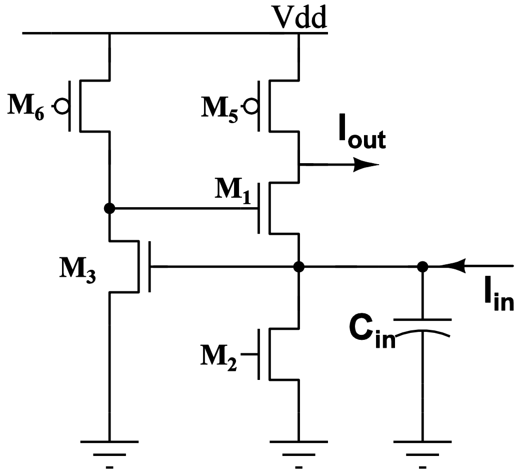

Fig. 21. G_m**-boosted common-gate current buffer**

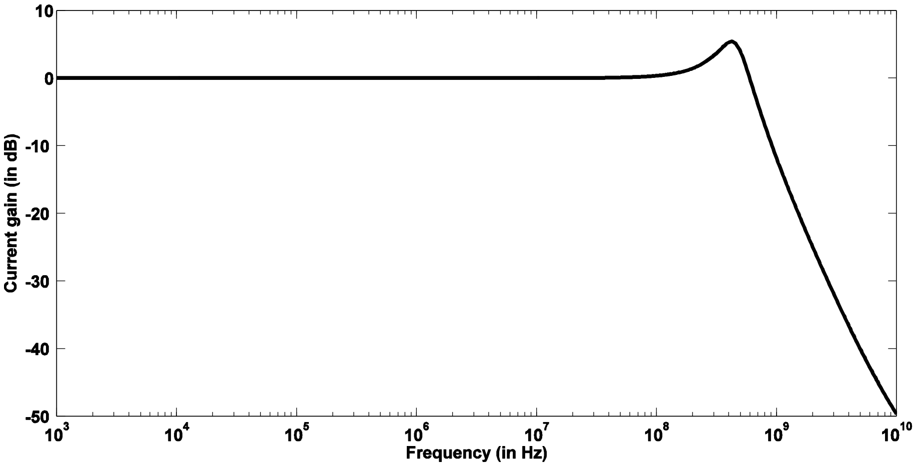

Fig. 22 Current gain of the g_m**-boosted common-gate current buffer**

The input impedance of the g_m-boosted common gate current buffer is derived as:

$$Z_{in} = \left[\frac{g_{m1}g_{m3}g_{ds5}}{(g_{ds1}+g_{ds5})[g_{ds3}+g_{ds6}]} + \frac{g_{ds5}}{g_{ds1}+g_{ds5}}(g_{m1}+g_{ds1}) + g_{ds2} + sC_{in}\right]^{-1} \tag{3.10}$$

If $g_{ds1}, g_{ds5}, g_{ds6}$ are very small, (3.10) can be simplified as,

$$Z_{in} = \left[\frac{g_{m1}g_{m3}}{g_{ds3}} + g_{m1} + g_{ds3} + sC_{in}\right]^{-1} = [g_{m1}(1 + g_{m3}r_{03}) + g_{ds3} + sC_{in}]^{-1} \tag{3.11}$$

It is observed that the g_{m1} is boosted by $(1 + g_{m1} r_{03})$ approximately, thereby decreasing input impedance by the same amount. An input capacitor, C_{in} is added to reduce the peaking of the impedance at medium to high frequencies. The input-referred current noise of the g_m-boosted common-gate current buffer is given by

$$I_{in,in}^2 = I_{n,M2}^2 + I_{n,M5}^2 + V_{n,M_3}(g_{m3} g_{m1}(r_{06}||r_{03}))^2 \tag{3.12}$$

where $V_{n,M_3} = \frac{4kT\gamma}{g_{m3}}$ is the voltage noise of the transistor M_3. The input-referred noise increases from a simple common-gate current buffer to a g_m-boosted common-gate current buffer, which is detrimental. However, by careful selection of bias currents through M_1 and M_3, this problem can be alleviated.

The common-gate current buffer is very linear [34] as long as the tail current source, which competes with the rest of the circuit for input current, has high impedance when compared to the input impedance of the current buffer. However, effects such as finite output impedance, non-linear transconductance and parasitic capacitances can affect the linearity of the buffer. Using the small-signal model in Fig. 23, we can express $V_{gs,M1}$ in terms of input impedance of current buffer, looking into the source of M_1 as

$$V_{gs,M1} = Z_{sg,M1} i_{d,M2} = \frac{Z_{ds,M1} + R_L}{1 + g_{m1,M1} Z_{ds,M1}} i_{d,M2} \tag{3.13}$$

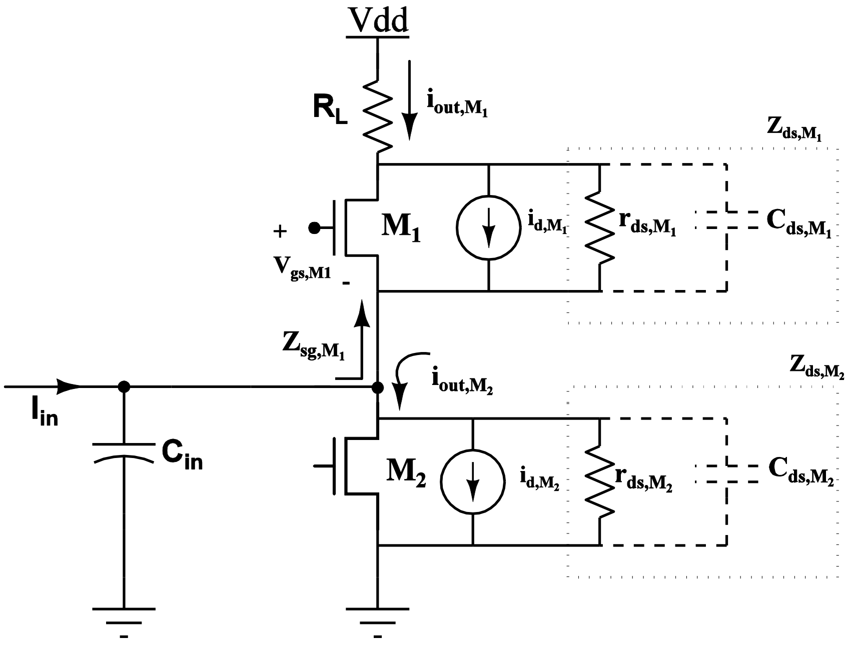

Fig. 23. Small signal model of a common-gate current buffer

The drain current ($i_{d,M1}$) of the transistor M$_1$ is given by

$$i_{d,M1} = g_{m1,M1}V_{gs,M1} + g_{m2,M1}V_{gs,M1}^2 + g_{m3,M1}V_{gs,M1}^3 + \cdots \tag{3.14}$$

where $g_{m2,M1}$, $g_{m3,M1}$ ... are non-linear contributions from transconductance of M_1. We can see from (3.13) that increasing the load resistance R_L increases $V_{gs,M1}$, thereby increasing the non-linear terms in (3.14). The non-linear currents produced due to finite output impedance of the current buffer, circulate inside the buffer in an ideal case. However, due to finite parasitic output capacitance, the non-linear currents leak, producing non-linearity at the output of the buffer. We can write the total output current $i_{out,M1}$ as a combination of drain current in M_2 and the leakage currents in M$_1$.

$$i_{out,M1} = i_{out,M2} = i_{d,M2} + \alpha i_{d,M1} \tag{3.15}$$

where $\alpha = \frac{Z_{sg,M1}}{Z_{sg,M1}+Z_{ds,M2}}$, which denotes the leakage ratio of non-linear currents in M_1. If $Z_{ds,M2} \gg Z_{sg,M1}$, α is negligible. This translates to having an efficient tail current source with large impedance when compared to the input impedance of the current buffer. However, at high frequencies, the parasitic capacitance at the source of M_1 becomes appreciable, increasing α, thereby degrading linearity. It could be explained qualitatively that as the non-linear currents leak through $Z_{dS,M2}$, an equal magnitude leakage current is produced at the output of the buffer to satisfy KCL.

3.3.3 Feedback current buffer

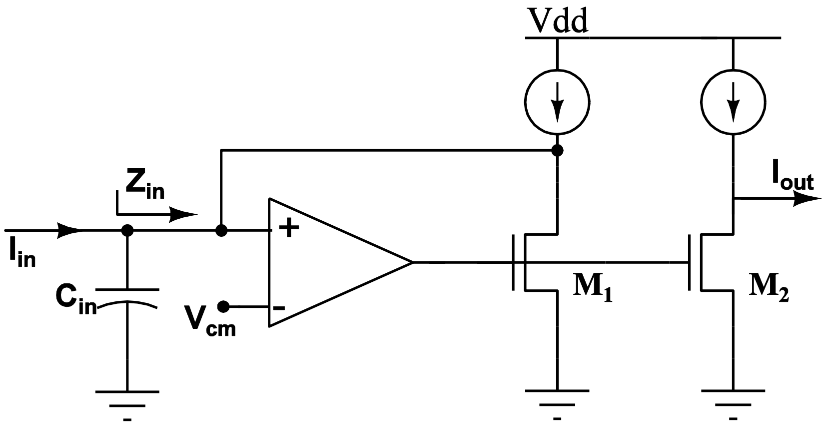

Fig. 24. Input Impedance of a feedback current buffer

The feedback current buffer is shown in Fig, 24, where the input impedance Z_{in} is decreased by the presence of negative feedback loop formed by the op-amp and the transistor M_1. The op-amp can be modeled as a single pole system with a finite gain A_0 and a ω_{3dB} cut-off frequency of ω_p, which has a gain transfer function as follows:

$$A(s) = \frac{A_0}{1 + \frac{s}{\omega_p}} \tag{3.16}$$

The current transfer function from input to output is given by

$$\frac{I_{out}}{I_{in}} = \frac{A(s)g_{m2}}{[sC_{in} + A(s)g_{m1}]} \tag{3.17}$$

From (3.17), we can see that if the transistors M_1 and M_2 are identical and the input capacitance C_{in} is neglected, the current transfer gain becomes approximately unity at low frequencies as plotted in Fig. 25.

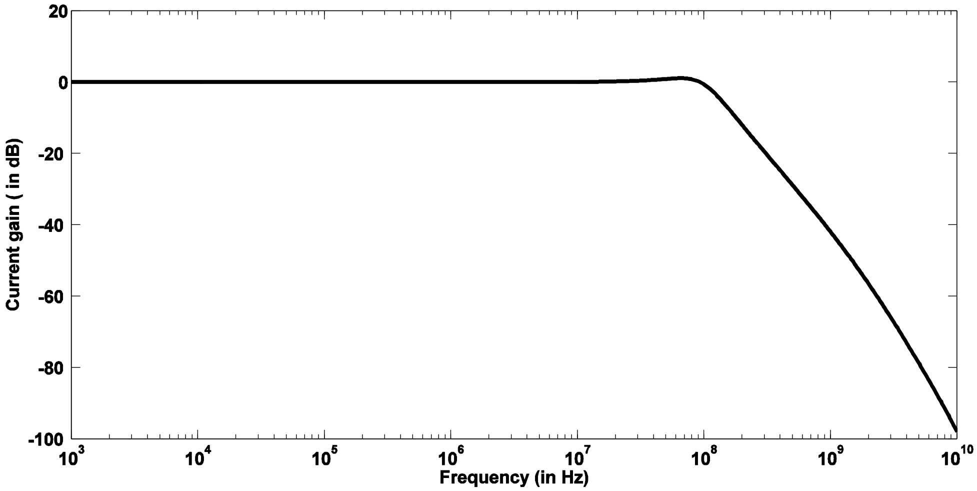

Fig. 25 Current gain of feedback current buffer

The input impedance of the feedback current buffer is given by

$$Z_{in} = \left[sC_{in} + g_{ds1} + g_{m1}\left(\frac{A_0}{1+\frac{s}{\omega_p}}\right)\right]^{-1} \tag{3.18}$$

The input-referred current noise for the feedback current buffer is given by

$$\begin{aligned} I_{in,in}^2 &= I_{n,M_1}^2\left(\frac{Ag_{m2}}{sC_{in}+Ag_{m1}}\right)^2 + I_{n,M_2}^2 + V_{n,opamp}^2 (\frac{(g_{m2}^2A_0^2)(sC_{in})^2}{(g_{m1}A_0+sC_{in})^2} \\ &\approx I_{n,M_1}^2 + I_{n,M_2}^2 + V_{n,opamp}^2(sC_{in})^2 \end{aligned} \tag{3.19}$$

We can see that the noise current of the transistor $M_1$is directly referred to the input along with the noise current of bias current source. The voltage noise of the op-amp, $V_{n,opamp}$ contributes almost zero noise at low frequencies. However, its contribution increases as the input capacitance starts sinking in more current to the ground.

Linearity is improved due to the feedback in the current buffer. The closed loop gain is relatively independent of an op-amp's open loop gain due to negative feedback. The loop gain of the feedback system shown in Fig. 24 is given by

$$A\beta(s) = A(s)g_{m1}R_{out} = \frac{A_0g_{m1}R_{out}}{\left(1+\frac{s}{\omega_p}\right)} \tag{3.20}$$

where R_{out} is the output impedance and it can be observed that the presence of the op-amp adds a pole to the loop gain. Therefore, having a simple op-amp with minimum poles in the transfer function is crucial for the feedback system to satisfy Barkhausen's stability criteria [26].

3.3.4 Current-mode third order minimally invasive filter

Figure 26 shows the current-mode third order minimally invasive filter which acts as the filtering stage of the baseband circuit in both the proposed architectures. To achieve third order lowpass filtering, Butterworth response was chosen and a third order Butterworth filter equation, when the input is current and the output is voltage is given by:

$$\frac{V_{out}}{I_{in}} = \frac{\omega_0{}^3 R_i}{s^3 + 2\omega_0 s^2 + 2\omega_0^2 s + \omega_0^3} \tag{3.21}$$

Comparing (3.21) with the general equation for a current-mode minimally invasive filter (1.13), we get the required impedance as:

$$Z_x = \frac{\omega_0^3 R_i}{s^3 + 2\omega_0 s^2 + 2\omega_0^2 s} \tag{3.22}$$

In (3.22), we see that the impedance Z_x needs to have three poles and no zeroes with its magnitude being infinity at DC. Therefore it needs to be predominantly a capacitive circuit. The designed impedance Z_x along with the resistor R_i forms the fully differential minimally invasive current-mode filter as shown in Fig. 26. The impedance Z_x in Fig.26 is derived as

$$Z_x = \frac{\frac{1}{R_1 R_2 C_1 C_2 C_f}}{s^2 + \frac{R_1 + R_2}{R_1 R_2 C_2} s^2 + \frac{C_1 + C_f}{R_1 R_2 C_1 C_2 C_f} s} \tag{3.23}$$

Comparing (3.23) with (3.22) we obtain following design conditions:

$$\omega_0 = \frac{1}{R C_2} \tag{3.24}$$

$$R = \frac{R_i C_1 C_f}{C_2^2} \tag{3.25}$$

$$\frac{C_1 + C_f}{C_1 C_f} = \frac{2}{C_2} \tag{3.26}$$

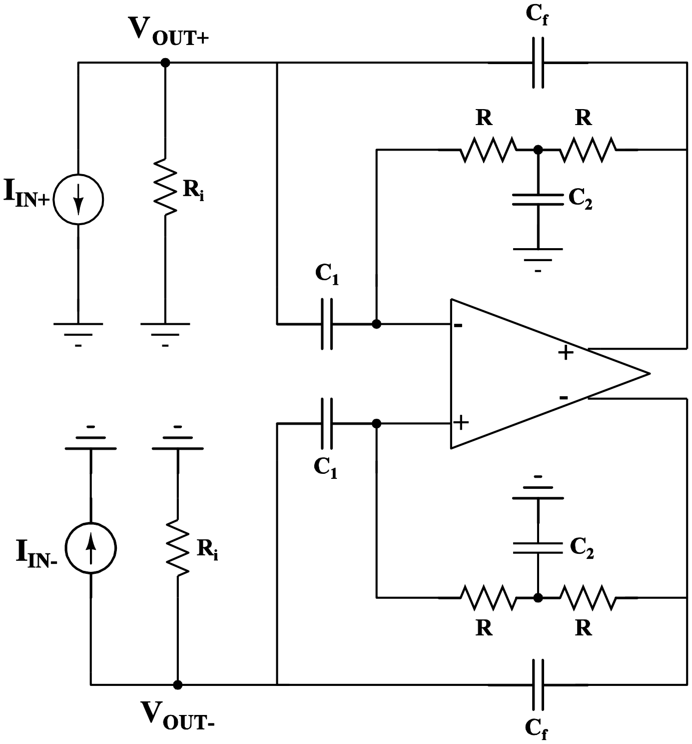

Fig. 26. Current-mode third order lowpass filter

The transfer function from I_{in} to the op-amp output node V_{o1} is given by

$$\frac{V_{o1}}{I_{in}} = \frac{\omega_0^3 (sRC_1)(2 + sRC_2)R_i}{s^3 + 2\omega_0 s^2 + 2\omega_0^2 s + \omega_0^3} \tag{3.27}$$

At ω_0, the above equation becomes

$$\left.\frac{V_{o1}}{I_{in}}\right|_{\omega=\omega_0} = \sqrt{\frac{5}{2}\frac{C_1}{C_2}}R_i \tag{3.28}$$

If we assume $C_1 = a_1C_2$ and $C_f = a_2C_2$, where a_1 and a_2 are two non-zero positive real variables then (3.26) becomes,

$$a_1 + a_2 = 2a_1a_2 \tag{3.29}$$

(3.25) and (3.28) are simplified as

$$R = R_ia_1a_2 \tag{3.30}$$

$$\left.\frac{V_{o1}}{I_{in}}\right|_{\omega=\omega_0} = \sqrt{\frac{5}{2}}a_1R_i \tag{3.31}$$

The value of RC_2 is determined by the desired ω_0 value. The values of a_1 and a_2 are chosen such that there is no peaking at the op-amp output node V_{o1}. For example if the output has a voltage swing of 0.4V, the input current would be 200μA for a transimpedance gain of $66dB\Omega$. For a voltage swing of 0.4V at the op-amp output node V_{o1}, (3.31) gives a value of 0.7 for a_1 and (3.27) is used to calculate the value of a_2 as 2.5 approximately.

Looking at the implementation of the filter itself, ω_0 of $10\ MHz$ was chosen for the third order minimally invasive lowpass Butterworth filter. As discussed in previous sections, to have a fair comparison with TIA-based first order implementation in [9], $R_i = 2K\Omega$ resistor was chosen, providing a transimpedance gain of $66dB\Omega$. From (3.24), (3.25) and (3.26), we obtain a_1 and a_2 as

$$a_1 = 0.63\,, a_2 = 2.42 \tag{3.32}$$

Therefore from (3.30),

$$R = R_i a_1 a_2 = 3.05k\Omega \tag{3.33}$$

From (3.24), $C_2 = \frac{1}{2\pi Rf}$ where $f = 10MHz,$ therefore $C_2 = 5.22\,pF.$ Since we assume $C_1 = a_1 C_2$ and $C_f = a_2 C_2,$ we obtain C_1 as $3.29\,pF$ and C_f as $12.62\,pF.$ A fully differential version of the filter has been implemented as shown in Fig. 26 and the design of the OTA required for the filter is discussed in detail in following sections.

3.4 Implementation of the baseband circuit

In this section, the transistor level implementation of the baseband circuit is discussed. Both of the proposed architectures, with the common-gate current buffer and the feedback current buffer have been implemented in TSMC $130nm$ technology. Both architectures use the same topology of the third order minimally invasive current-mode Butterworth filter. The results with transistor level schematics are compared and the architecture with optimum performance metrics has been chosen to be implemented on silicon.

3.4.1 Baseband circuit with common-gate current buffer

Figure 27 shows the schematic of the baseband circuit with common-gate current buffer. A pseudo-differential common-gate current buffer is fed into a fully differential minimally invasive filter. The fully differential third order filter's passive input resistors R_i are connected together to form a virtual ground. The transimpedance equation from input to output is given by

$$\frac{V_{out}}{I_{in}} = \frac{g_{m1}\left(1 + g_{m3}(g_{ds6} + g_{ds3})\right)}{\left[(g_{ds2} + sC_{in}) + g_{m1}\left(1 + g_{m3}(g_{ds6} + g_{ds3})\right)\right]} \frac{R_i Z_x}{R_i + Z_x}$$
$$\approx \left(\frac{R_i Z_x}{R_i + Z_x}\right) \tag{3.34}$$

where Z_x is the synthesized frequency dependent impedance. The current gain of the buffer is approximately unity in the baseband frequency range where the minimally invasive filter operates, thereby enabling us to approximate the transimpedance equation as calculated in (3.34).

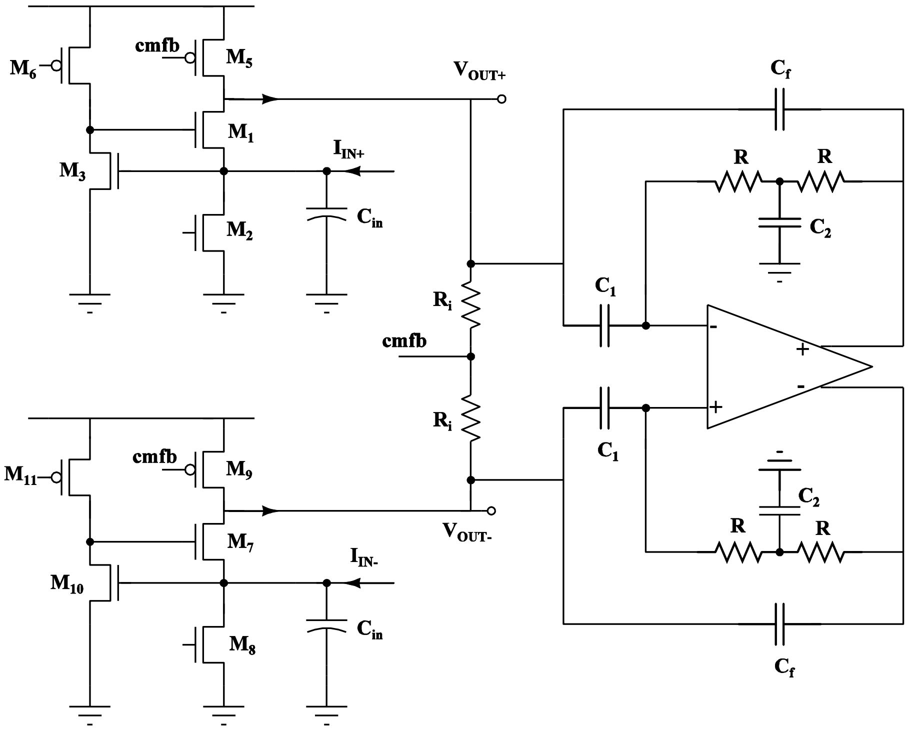

Fig. 27. Baseband circuit with common-gate current buffer

The common mode voltage level at the output is maintained by the common mode feedback circuit (CMFB), which makes use of the node $cmfb$ as shown in Fig. 27. No common mode current flows through the resistors R_i since both the current buffer circuits are identical and the DC voltage at the nodes V_{OUT+} and V_{OUT-} is made equal by the simple feedback loop controlling the current through the PMOS transistors M_5 and M_9 by adjusting their gate voltage. While designing the current buffer, care has been taken to select an optimum bias current in the main input stage and an optimum gain for the g_m-booster circuit so that we obtain a trade-off between input-referred noise (which depends directly on the bias current as discussed in the previous section) and the input impedance of the circuit. A bias current of 250 μA has been used in the main input transistor branch with another 250 μA in the g_m-booster branch. The NMOS input transistor was selected since NMOS transistors generally have a higher transconductance for the same bias current, which enables us to have a lower input impedance since it is inversely proportional to g_m. The PMOS current source for the buffer has been implemented as a simple current source due to headroom limitations because of a power supply of 1.2V. A 20pF input capacitor was used to reduce the peaking of input impedance at higher frequencies. The table III shows the transistor sizes for the current buffer.

Table III Transistor sizes for common-gate current buffer

Transistor	**Width per finger**	**Length**	**Fingers**
M_1, M_7	5.8μ	0.13μ	4
M_2, M_8	13.5μ	0.9μ	4
M_3, M_{10}	9μ	0.3μ	4
$M_{5,}M_9$	17.5μ	0.3μ	4
M_6, M_{11}	9.6μ	0.3μ	4

3.4.2 Baseband circuit with feedback current buffer

The schematic of the baseband circuit with the feedback current buffer is shown in Fig. 28. The input current signal is fed into a negative feedback loop formed by the op-amp and the common source structure with a PMOS cascode current mirror. The fully differential third order filter's passive resistors R_i are connected together to form a virtual ground. The transimpedance equation from input to output is given by

$$\frac{V_{out}}{I_{in}} = \left(\frac{A(s)g_{m2}}{[sC_{in} + A(s)g_{m1}]}\right)\left(\frac{R_i Z_x}{R_i + Z_x}\right) \approx \left(\frac{R_i Z_x}{R_i + Z_x}\right) \tag{3.35}$$

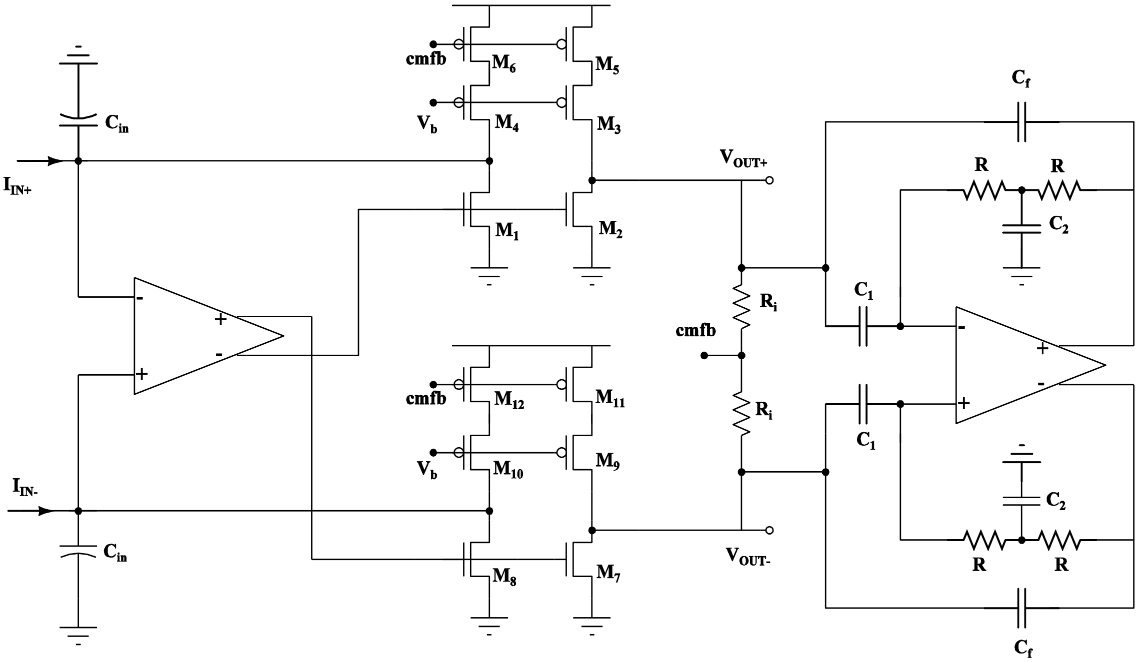

Fig. 28. Baseband circuit with feedback current buffer

The current gain of the feedback current buffer is approximately unity in the baseband range similar to the common-gate buffer discussed in the previous section. From Fig. 28, we can notice that the CMFB circuit follows the same principle as the CMFB circuit in previous section, using the virtual ground $cmfb$ to maintain output common mode levels. The feedback loop consisting of the op-amp and the common source stage needs to have sufficient phase margin. Therefore, the op-amp needs to have a low to moderate voltage gain with careful positioning of the poles so that the feedback loop is stable. A current mirror fully differential OTA shown in Fig. 29 has been used to achieve a small signal gain of $24.9dB$ with a GBW of $225MHz$ for a load capacitance of $10\ pF$. The OTA has a phase margin of 85° in a unity gain feedback loop configuration.

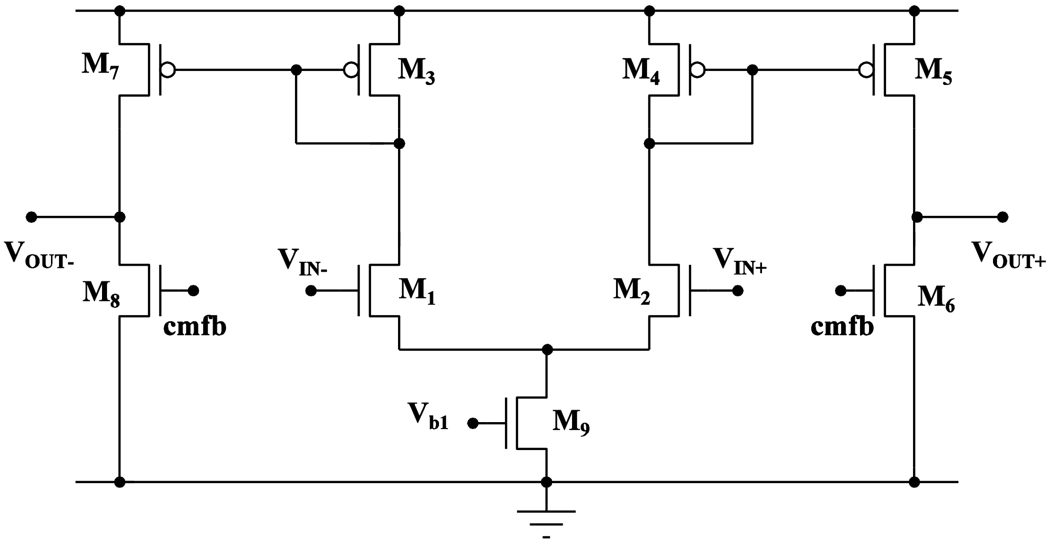

Fig. 29 Block diagram of the current mirror OTA

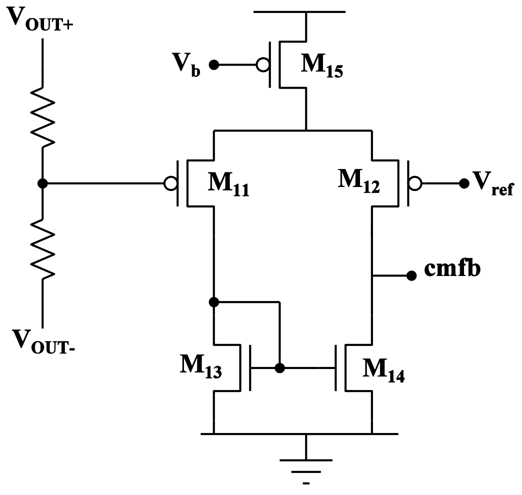

Fig. 30 CMFB circuit for the OTA

The G_m of the OTA in Fig. 29 can be enhanced by having a higher current mirror ratio from M_4 to M_5. The effective G_m becomes βg_{m1} where β is current mirror ratio (between M_4 and M_5) and g_{m1} is transconductance of input transistor M_1. A PMOS input stage has been used to reduce flicker noise and the output stage has a CMFB circuit to maintain the output common mode level at the designed value of $500mV$. The CMFB circuit is a simple single ended differential amplifier as shown in Fig. 30, with a resistive path for common mode detection and an op-amp for common mode error correction. The CMFB circuit consumes a current of $250\mu A$. Figure 31 shows the frequency response of the OTA while the table IV summarizes the performance of the current mirror OTA with a load capacitance of $10pF$. Figure 32 plots the loop gain and phase for the feedback loop formed by the OTA and the input transistor M_1. The loop gain is $71dB$ approximately with a phase margin of 55°. The linearity improves because of the negative feedback loop as discussed in the previous section.

Table IV Performance summary for the current mirror OTA

Parameter	**Value**
DC gain	24.90 dB
GBW	225 MHz
Phase margin (in unity-gain feedback loop)	85°
Integrated Input-referred noise (from 0.01Hz to 10MHz)	29.92 μV
Power Consumption	3.48mW

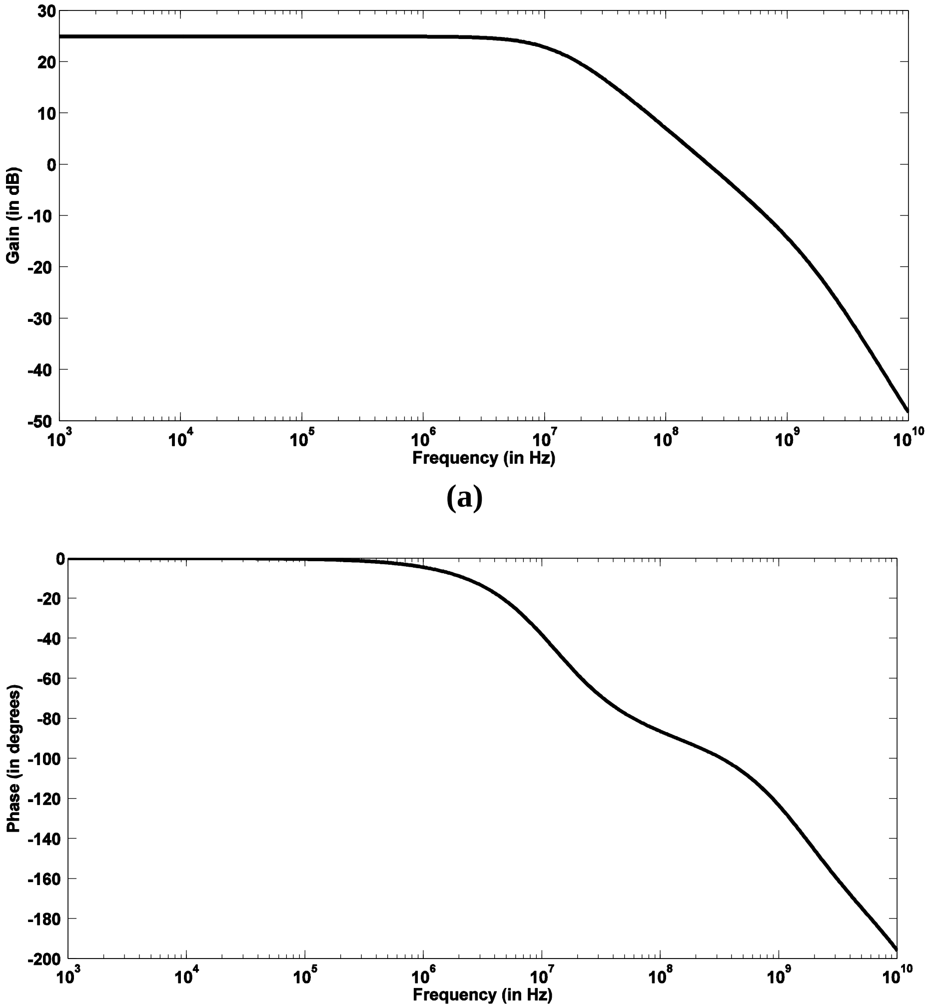

(a)

(b)

Fig. 31 Frequency response of the current mirror OTA (a) Gain (b) Phase

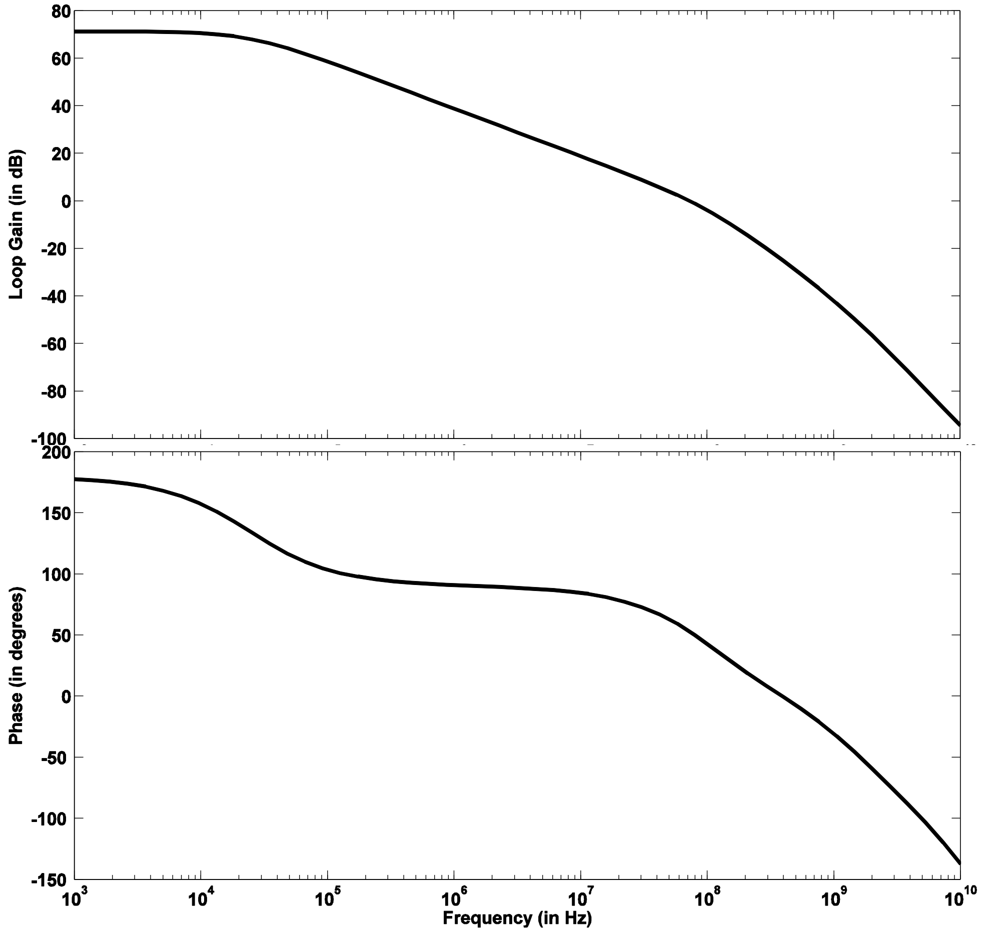

Fig. 32 Loop gain and phase for the feedback loop

A bias current of 166 μA has been used in the main input transistor branch with another 166 μA in the current mirror output branch. As discussed in the common-gate current buffer based baseband circuit architecture, NMOS input transistors were used to have lesser input impedance with an input capacitor of $50\,pF$ to compensate for the peaking in input impedance at higher frequencies. Table V shows the transistor sizes for the current buffer.

Table V Transistor sizes for feedback current buffer

Transistor	**Width per finger**	**Length**	**Fingers**
M_1, M_2, M_7, M_8	9μ	1.8μ	4
M_3, M_4, M_9, M_{10}	24μ	0.3μ	3
M_5, M_6, M_{11}, M_{12}	16μ	0.9μ	3

3.4.3 Design of the OTA for the minimally invasive filter

A two-stage feed-forward compensated OTA has been designed to be used for the current-mode minimally invasive filter. The two-stage architecture has been chosen to achieve a moderate gain and a high gain bandwidth product so that zero present inherently in the design of the filter moves to high frequencies. Instead of a traditional Miller compensation, a feed-forward transistor based compensation has been used, which does not split the poles and the ω_{3dB} bandwidth of the op-amp is extended when compared to Miller compensation based implementation. Moreover, the Miller compensation with a nulling resistor requires higher power to achieve the same GBW as a feed-forward compensation based implementation. Figure 33 shows the block diagram of a feed-forward two-stage OTA [35]. The feed-forward path due to g_{m3} (M_3 and M_5 in Fig. 34) introduces a left half plane (LHP) zero, which compensates the two RHP poles produced by the cascaded common-source amplifiers, which produce negative phase shift for the OTA.

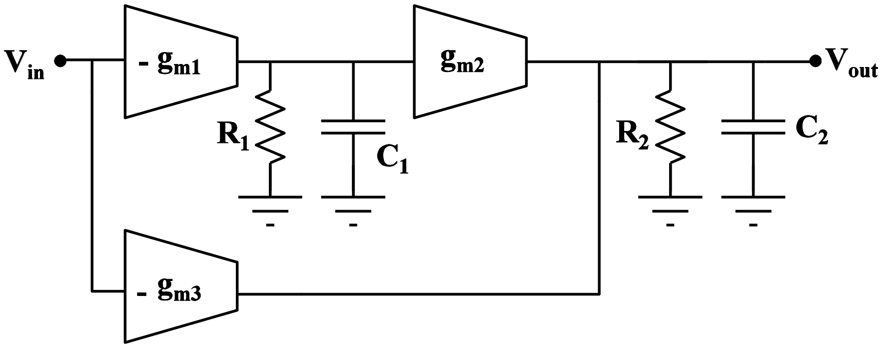

Fig. 33 Block diagram of the feed-forward OTA

By compensating using a feed-forward scheme, a desired phase margin is obtained without using passives such as compensation capacitors or resistors. The voltage transfer function from input to output for the OTA is given by

$$\frac{V_{out}}{V_{in}}(s) = \frac{(A_1A_2 + A_3)\left(1 + \frac{A_3 s}{(A_1A_2 + A_3)\omega_{p1}}\right)}{\left(1 + \frac{s}{\omega_{p1}}\right)\left(1 + \frac{s}{\omega_{p2}}\right)} \qquad (3.36)$$

where A_1, A_2, A_3 are the low-frequency voltage gains of the first, second and feed-forward stages and $\omega_{p1}, \omega_{p2}$are the RHP poles produced due to cascade of first and second stages of amplifiers. We can see from the equation (3.37) that the feed-forward stage adds a zero in the numerator for the transfer function, which improves the phase response of the OTA.

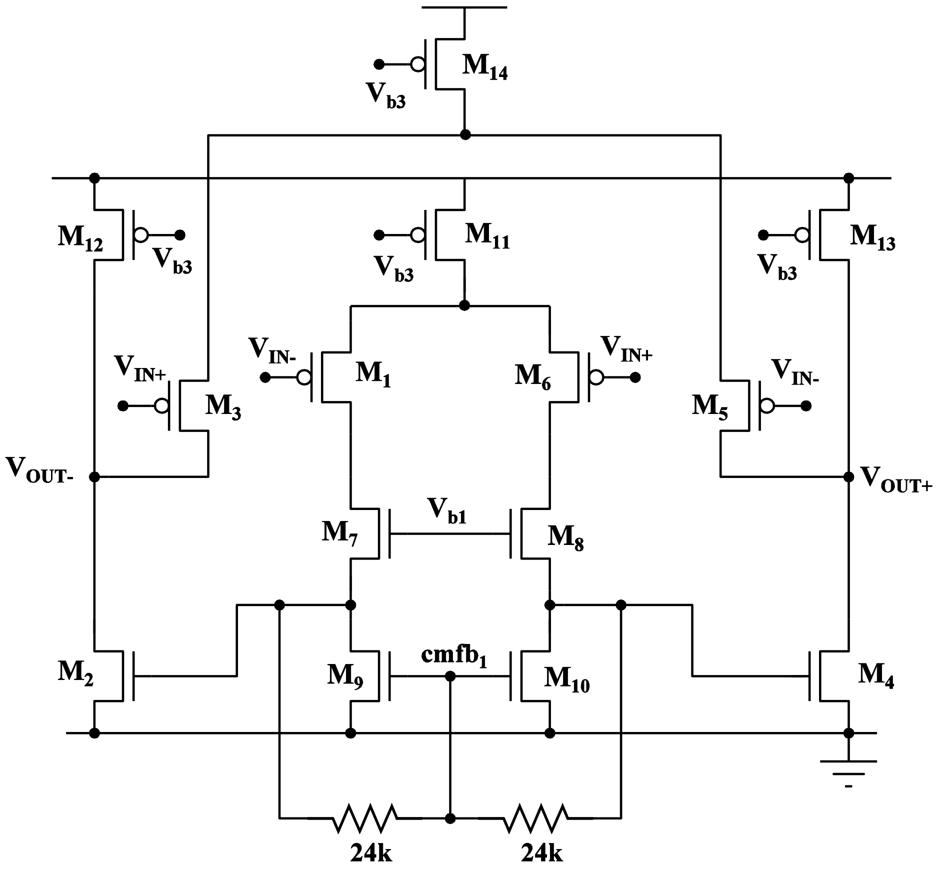

Fig. 34 Schematic of the feed-forward OTA

The schematic of the designed OTA is shown in Fig. 34. It has a PMOS differential input stage for lower flicker noise followed by a NMOS input stage with a feedforward stage formed by transistors $M_3$and M_5. For the first stage, the common mode output voltage level is maintained by a simply connecting resistors from drain of transistors M_9 and M_{10} to their gate at $cmfb_1$. The common mode voltage level at the second stage is controlled by a CMFB circuit shown in Fig. 35. Resistors are used to sense the common mode voltage and the transistors M_{21} and M_{22} work for common mode correction.

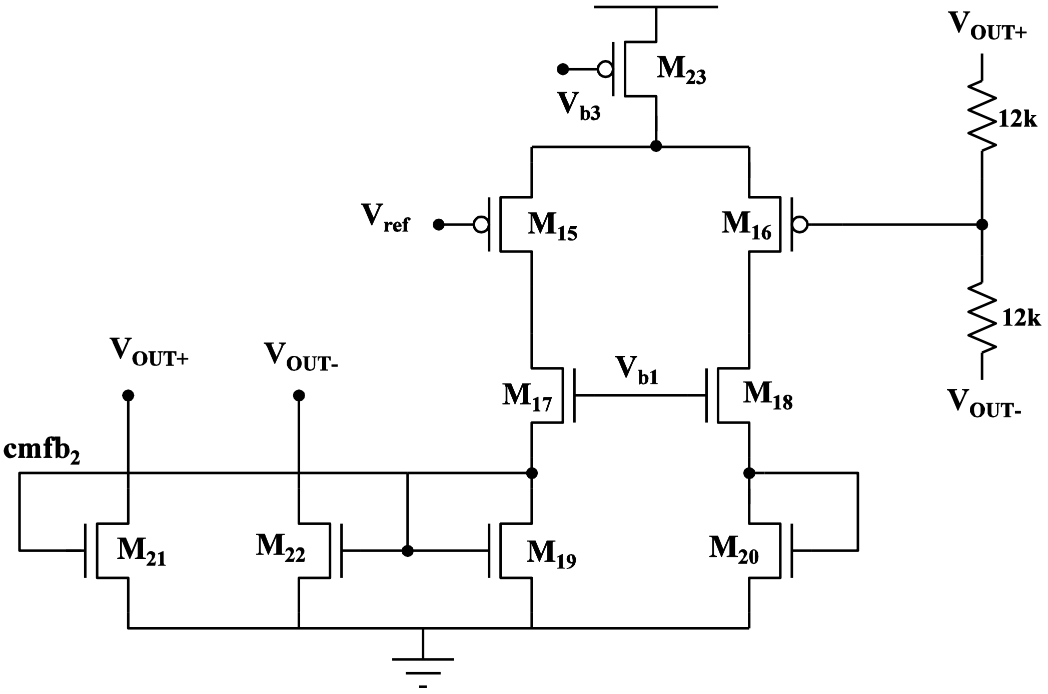

Fig. 35 CMFB for the feedforward OTA

Compensating the OTA using an active feed-forward stage puts pressure on noise and power consumption while alleviating area used. The input-referred noise of the OTA is given by

$$V_{n,in}^{2} = 8kT\frac{\gamma}{\alpha}\left(\frac{1}{g_{m1}} + \frac{g_{mn}}{g_{m1}^{2}} + \frac{g_{m2} + g_{m3} + g_{mp}}{(A_{1}g_{m2})^{2}}\right) \tag{3.37}$$

We can see that the noise due to the feed-forward stage g_{m3} is scaled down by the gain of the first stage $A_{!}$ at low frequencies. The designed OTA has a small signal DC gain of $48dB$ for a GBW of $2.63GHz$. The phase margin is 65°. The frequency response plot showing the voltage gain of the OTA is given in Fig. 36.

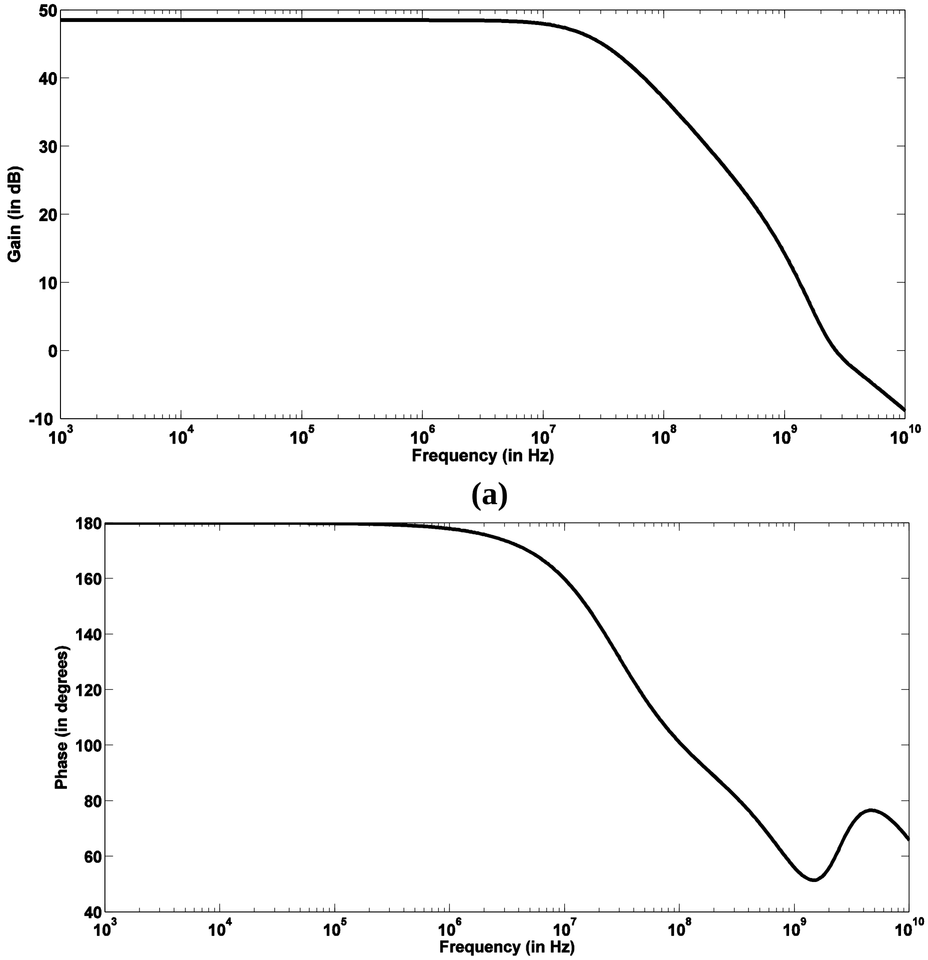

(a)

(b)

Fig. 36 Frequency response of the feed-forward OTA (a) Gain (b) Phase

Table VI summarizes the performance of the feed-forward OTA

Table VI Performance metrics for the feed-forward OTA

Parameter	**Value**
DC gain	48.5 dB
GBW	2.63 GHz
Phase margin	65.49°
Integrated Input-referred noise (from 0.01Hz to 10MHz)	17.54μV
Power Consumption	3.78mW

3.5 Simulation setup and results

In this section, schematic level simulation results for both architectures are discussed. Since the reference design of the TIA was only a first order implementation in [27], a third order filter has been implemented by using a TIA with first order filtering along with a Tow-Thomas biquad (reference for the second order portion of the filter) in cascade. The Tow-Thomas biquad has a good linearity and could be implemented differentially, which would be an appropriate comparison with the minimally invasive counterpart. The second order Tow-Thomas biquad along with first order TIA uses three OTAs in its design, and a fully-differential version has been implemented as shown in Fig. 37. For the Tow-Thomas biquad, transfer function for the second order portion of the circuit is given by

$$H(s) = \frac{\left(\frac{R_2}{R_1}\right)\omega_0^2}{s^2 + \frac{\omega_0}{Q}s + \omega_0^2} \tag{3.38}$$

$$where\ \omega_0 = \sqrt{\frac{1}{R_2R_4C_1C_2}} \qquad and\ Q = \sqrt{\frac{R_3^2C_1}{R_2R_4C_2}}$$

If we consider all the resistor components $R_1 = R_2 = R_3 = R_4 = R_x$ and capacitor components $C_1 = C_2 = C_x$, then the transfer function in (3.38) becomes

$$H(s) = \frac{\omega_0^2}{s^2 + \frac{\omega_0}{Q}s + \omega_0^2} \tag{3.39}$$

where $\omega_0 = \frac{1}{R_xC_x}$ and $Q = 1$.

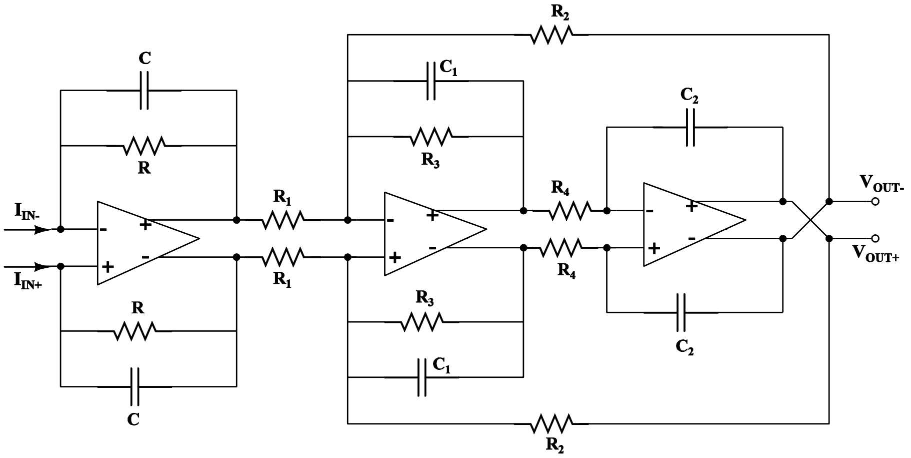

Fig. 37 Third Order Filter using TIA and Tow Thomas biquad

Since we need to implement a third order lowpass Butterworth filter, we can split the third order filter equation into two parts as

$$\frac{V_{out}}{I_{in}} = \frac{\omega_0^3 R}{s^3 + 2\omega_0 s^2 + 2\omega_0^2 s + \omega_0^3} = \left(\frac{\omega_0 R}{s + \omega_0}\right)\left(\frac{\omega_0^2}{s^3 + \omega_0 s + \omega_0^2}\right) \qquad (3.40)$$

By equating the second order equation with (3.39) for a ω_0 of $10MHz,$ we get the values of R_x and C_x as $R_x = 2k\Omega$ and $C_x = 7.95pF$. The first order equation is implemented by the TIA itself, which has a feedback resistor and capacitor to implement the first order filter. By equating first order equation with (3.2), we obtain the values of R and C as $2k\Omega$ and $7.95pF$. The baseband circuit formed with the first order TIA and the Tow Thomas biquad (TIA-biquad) is compared with the baseband circuit formed with the minimally invasive filter using the two architectures mentioned below:

a. Baseband circuit with common-gate current buffer. (CG-MINV)
b. Baseband circuit with feedback current buffer. (Feedback-MINV)

Figure 38 shows the frequency response of the baseband circuits for all the three baseband circuits: CG-MINV, feedback-MINV and TIA-biquad. The low frequency gain is $66dB\Omega$ and the ω_{3dB}cut-off frequency is $10MHz$ for the Butterworth lowpass filter implementation. The feedback-MINV structure has better high frequency attenuation compared to CG-MINV baseband circuit because of the higher capacitance at the input. All the designed baseband circuits show third order roll-off after the ω_{3dB} cut-off frequency with a Butterworth lowpass response.

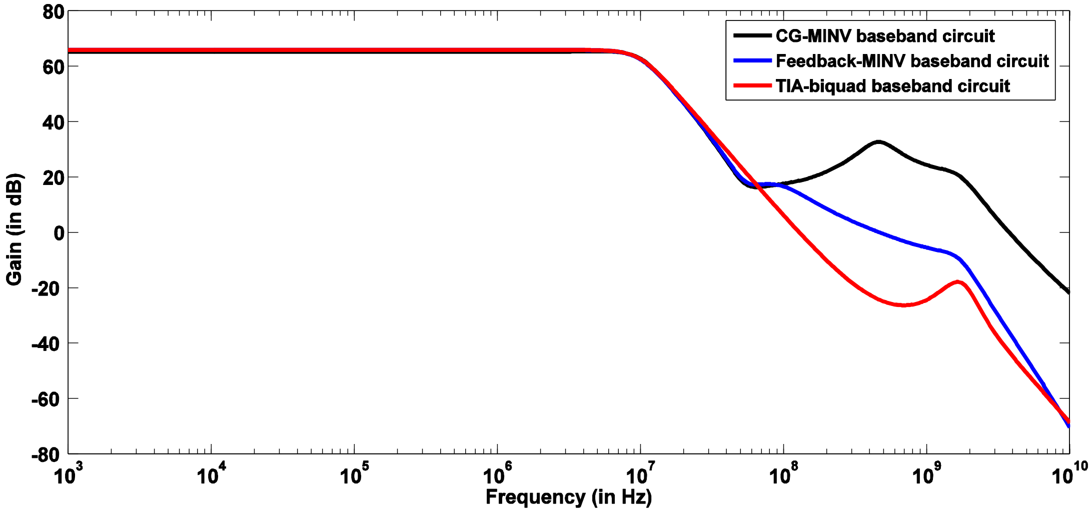

Fig. 38 Frequency response of the baseband circuits

The minimally invasive based baseband circuits have LHP zeroes at high frequencies, which contribute to their peaking in frequency response. This can be attenuated by using large off-chip capacitors at the input of the baseband circuit. Figure 39 shows the frequency response of baseband circuits when a $100\ pF$ capacitor has been added to the input of minimally invasive based baseband circuits. We can see that the peaking has been reduced at high frequencies. However, the linearity of the minimally invasive filter-based baseband circuits is comparable to the conventional third order baseband circuit even with the presence of zeroes at higher frequencies, which is discussed in detail with linearity plots. Therefore all the other results and the layout has been done without the off-chip capacitor since the zeroes do not degrade any performance parameter significantly.

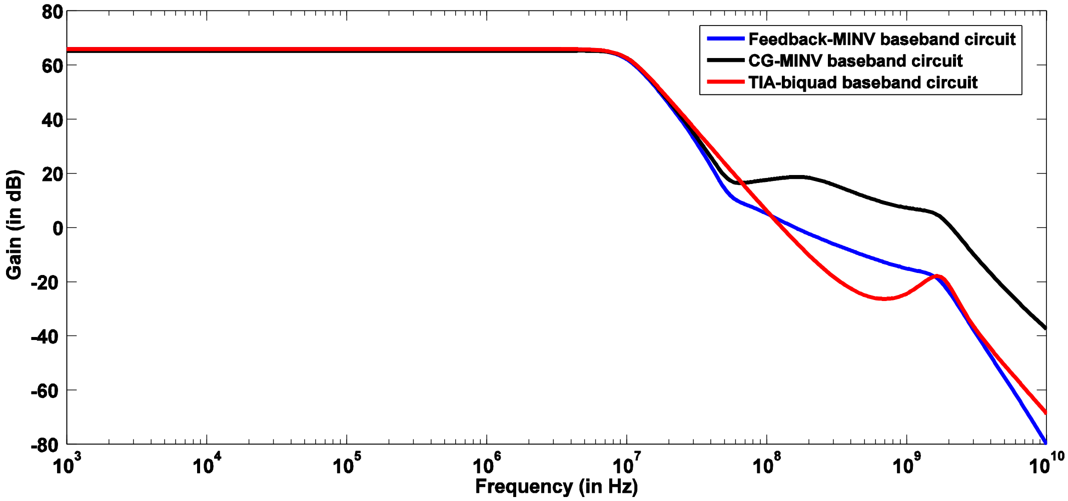

Fig. 39 Frequency response of baseband circuits (With large input capacitor for MINV based baseband circuits)

The input impedance of the baseband circuits is plotted in the Fig. 40. We can see that the CG-MINV circuit has least peaking at high frequencies and lowest magnitude in general.

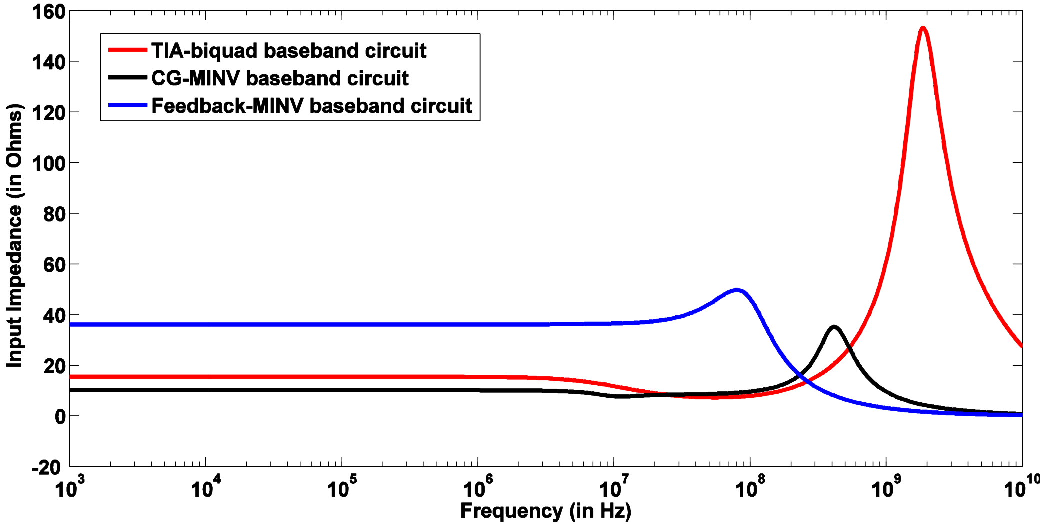

Fig. 40 Input Impedance of baseband circuits

The input-referred current noise for the three baseband circuits is plotted in Fig. 41. We can see that the TIA-biquad circuit has higher low frequency input-referred noise while the broad-band noise is approximately equal in all the three circuits.

The linearity of the baseband circuits is measured by two-tone test across different frequencies along with operating range of the circuit. It is important to note that blocker rejection at frequencies outside ω_{3dB}cut-off frequency of the baseband circuit becomes crucial. When one of the tones (f_1) is set as $10MHz$, the other tone (f_2) is swept from $12.5MHz$ to $20MHz$ and the power of the output signal at folded back frequency, which is in-band for the circuit, is plotted in Fig. 42. Similarly, when $f_1 = 30MHz$, the other tone f_2 is swept from $50MHz$ to $60MHz$ to obtain attenuation of various in-band folded back tones for the circuit, which is plotted in Fig. 43. Table VII summarizes the values for all the baseband circuits.

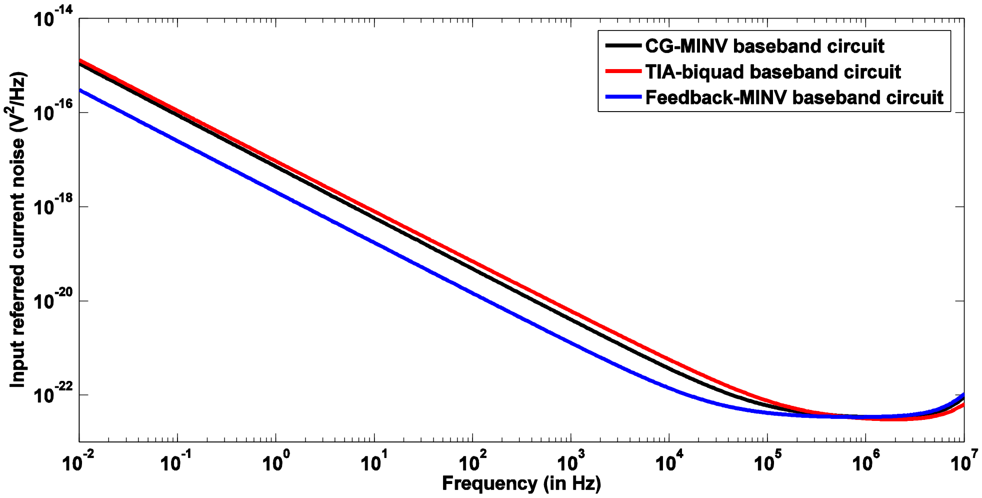

Fig. 41 Input-referred current noise for the baseband circuits

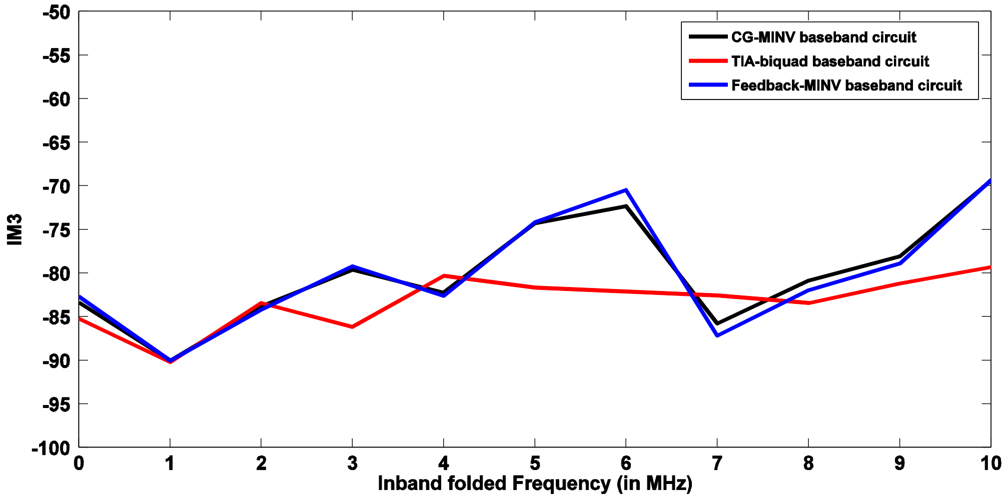

Fig. 42 IM_3 vs folded back frequency for the baseband circuits

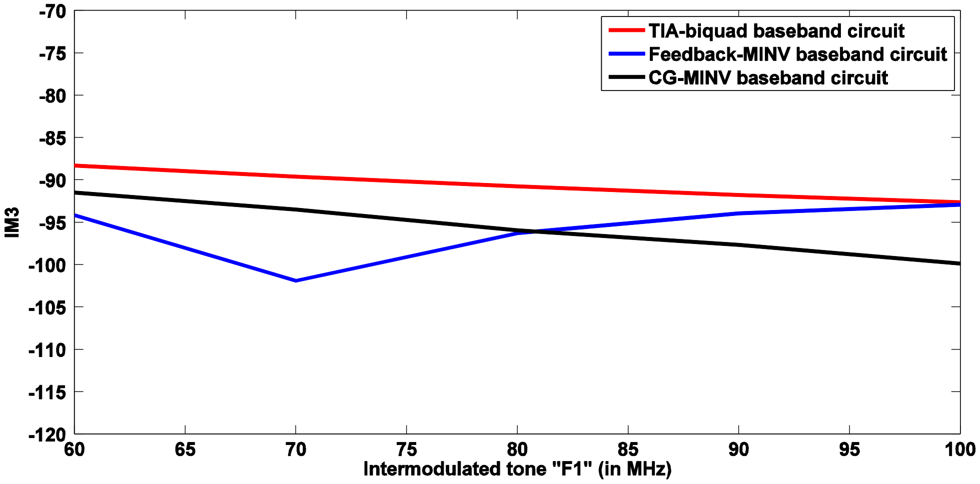

Fig. 43 IM_3 vs f_2 (when $f_1 = 30MHz$) for baseband circuits

To account for the presence of zeroes at higher frequencies, linearity has been quantified at higher frequencies by measuring the IM_3 of the folded back signal when two-tone test is perfomed at higher frequencies. Fig. 43 shows the IM_3 values at a folded back frequency of $5MHz$, which is in-band for the circuit when f_1 is swept from $60MHz$ to $100MHz$ and other tone f_2 is swept from $115MHz$ to $195MHz$ suct that the folded back frequency remains at $5MHz$. Simiarly, two-tone test is performed when f_1 varies from $350MHz$ to $400MHz$ while f_2 varies from $695MHz$ to $795MHz$ so that the folded back frequency remains at $5MHz$ to produce the IM_3 plots as shown in Fig. 44. The IM_3 plots show that minimally invasive based baseband circuits show linearity figures similar to each other, even at high frequencies. After simulating the baseband circuits, the reference receiver design in [27] has been used to simulate the integrated receiver chain with the designed baseband circuit. The first order TIA after the mixer has been replaced with all the three designed baseband circuits: CG-MINV, Feedback-MINV and TIA-biquad to compare the net noise figure and conversion gain for the receiver.

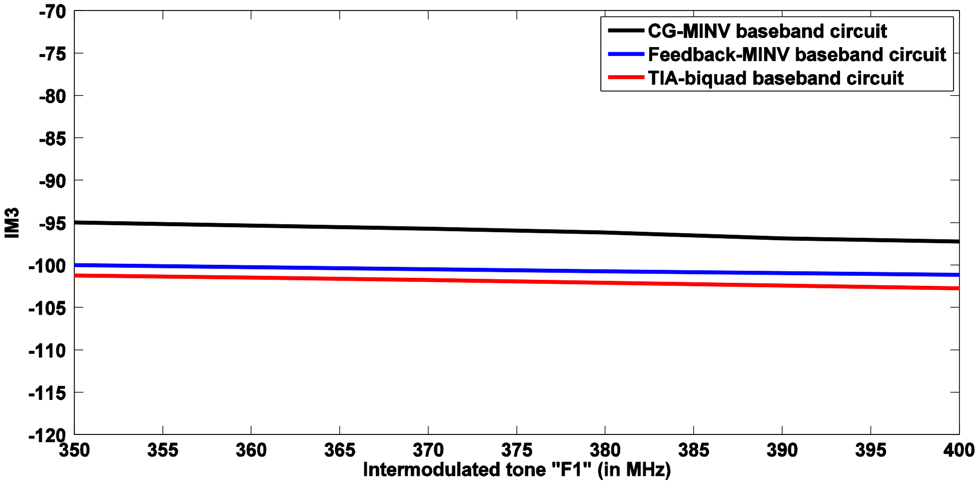

Fig. 44 IM_3 vs f_1 (350MHz to 400MHz) for baseband circuits

Figure 45 shows the noise figure for the receiver with all the three baseband circuits, where we can see that the receiver with CG-MINV baseband circuit shows the minimum noise figure. Figure 46 shows the magnitude of the signal at inter-modulated in-band frequency when one of the tones f_1 is at $30MHz$, the other tone f_2 is swept from $50MHz$ to $60MHz$. The IM_3 values are summarized in table VIII. Table IX summarizes the simulation results for the receiver with the three baseband circuits where the conversion gain is measured at an LO frequency of $6GHz$.

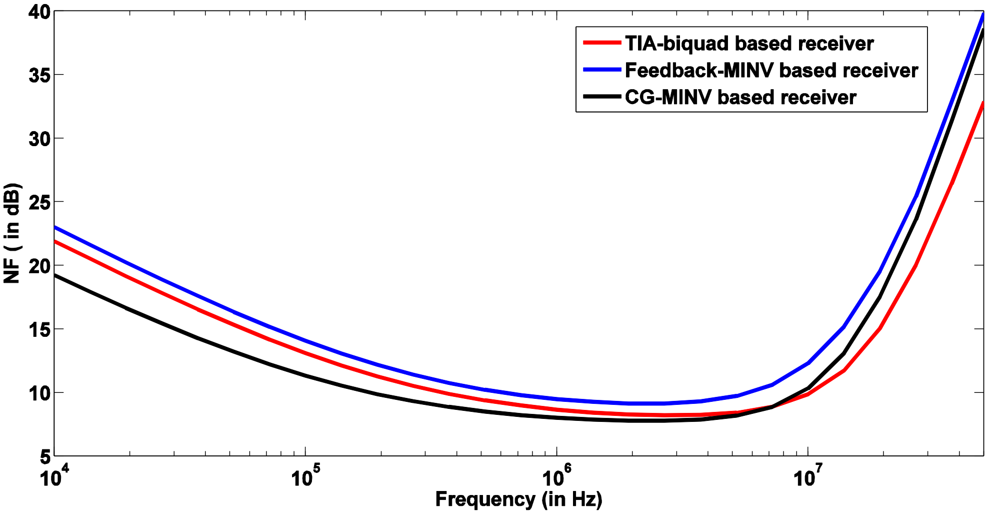

Fig. 45 Noise figure of the receiver with baseband circuits

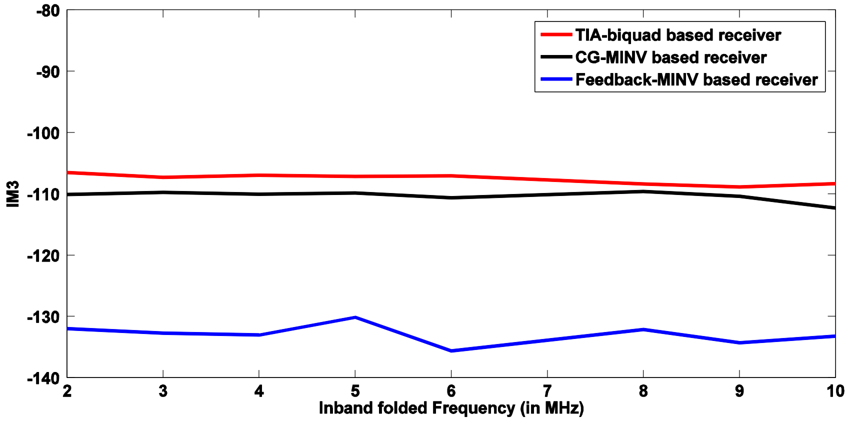

Fig. 46 IM_3 vs folded back frequency for the receiver with baseband circuits

Table VII Schematic results summary for the baseband circuits

Parameter			**CG-MINV**	**Feedback-MINV**	**TIA-biquad**
Low frequency gain (in dBΩ)			65.21	65.83	65.89
ω_{3dB}cut-off frequency			10.19 MHz	9.75 MHz	9.77 MHz
Linearity	F_1	F_2	IM_3 (in dB)		
	(in MHz)				
	8	9	-77.26	-81.30	-81.52
	9.8	10.2	-83.74	-95.91	-89.54
	10	12.5	-67.66	-74.17	-72.29
	10	15	-81.23	-81.57	-82.10
	10	17.5	-76.25	-73.37	-73.32
	10	18	-77.49	-73.38	-74.21
	30	50	-69.38	-79.29	-69.30
	30	51	-78.09	-81.20	-78.91
	30	52	-80.84	-83.42	-81.97
	30	53	-85.81	-82.57	-87.21
	30	54	-72.31	-82.12	-70.46
	30	55	-74.26	-81.68	-74.14
	30	56	-82.23	-80.30	-82.61
	30	57	-79.63	-86.17	-79.20
	30	58	-83.80	-83.40	-84.20
	30	59	-90.05	-90.24	-90.04
	30	60	-83.40	-85.20	-82.71
	60	115	-91.48	-94.15	-88.31
	70	135	-93.51	-101.88	-89.62
	80	155	-95.94	-96.28	-90.77
	90	175	-97.66	-93.94	-91.77
	100	195	-99.88	-92.91	-92.66
	350	695	-94.98	-100.01	-101.21
	360	715	-95.33	-100.25	-101.47
	370	735	-95.72	-100.49	-101.77
	380	755	-96.15	-100.72	-102.08
	390	775	-96.85	-100.94	-102.40
	400	795	-97.23	-101.16	-102.73
Input-referred integrated Noise (from 0.01Hz to 10MHz)			24.30 nV	24.12 nV	23.12 nV

Table VII Continued

Parameter		**CG-MINV**	**Feedback-MINV**	**TIA-biquad**
Input Impedance	**At Low frequency**	10.17 Ω	36.14 Ω	15.46 Ω
	Maximum value (peaked)	35.19 Ω	49.81 Ω	153 Ω
Power Consumption (W)		6.17m	9.36m	11.36m
Area (Differential implementation)		42.3pF,16K 40pF at input	42.3pF,16K 100pF at input	47.7pF,6K

Table VIII Two tone test for the receiver with baseband circuits

	F_1	F_2	**CG-MINV**	**Feedback-MINV**	**TIA-biquad**
	(in MHz)		IM_3 (in dB)		
Linearity	30	50	-112.31	-133.21	-108.36
	30	51	-110.39	-134.32	-108.9
	30	52	-109.62	-132.12	-108.37
	30	54	-110.65	-135.63	-107.08
	30	55	-109.85	-130.12	-107.16
	30	56	-110.05	-133.01	-106.98
	30	57	-109.77	-132.74	-107.31
	30	58	-110.08	-131.98	-106.54

Table IX Summary of results for the receiver with baseband circuits

Parameter	**CG-MINV**	**Feedback-MINV**	**TIA-biquad**
Conversion Gain (in dB)	26.49	25.50	27.11
Noise Figure (in dB)	7.77	9.65	8.68
Power Consumption (W)	15.37m	18.56m	20.56m

3.6 Analysis of simulation results and layout considerations

From table VII, we can see that the linearity of the CG-MINV baseband circuit is similar to the TIA-biquad circuit whereas the Feedback-MINV circuit reports a higher linearity for the same two-tone test. However, note that the power consumption of the CG-MINV circuit is almost half of that of the conventional TIA-biquad circuit. The input-referred current noise, when integrated from $0.01Hz$ to $10MHz$ is almost similar in all the three circuits. Therefore, we can conclude that though the feedback-MINV circuit has higher linearity, the CG-MINV circuit offers almost similar performance measures on linearity and noise with half the power consumption. Also, when we compare the area used for the three circuits in the table X, it can be seen that CG-MINV circuit has smaller input capacitance when compared to feedback-MINV circuit. Moreover, from the receiver performance results with different baseband circuits, we can see that the Feedback-MINV circuit has the highest input impedance as seen from Fig. 40, which degrades the performance of the mixer. Also, we can see that CG-MINV baseband circuit offers less noise figure with half the power consumption when compared to the conventional solution.

Table X Area comparison of baseband circuits

Parameter	**CG-MINV**	**Feedback-MINV**	**TIA-biquad**
Area (Differential circuit)	42.3pF,16K and 40pF at input	42.3pF,16K and 100pF at input	47.7pF,6K

From the above discussion, we can conclude that CG-MINV circuit offers optimum performance on linearity, noise, power consumption and filtering. Therefore, CG-MINV circuit has been designed on TSMC $130nm$ technology along with the TIA-biquad circuit for post-layout comparison.

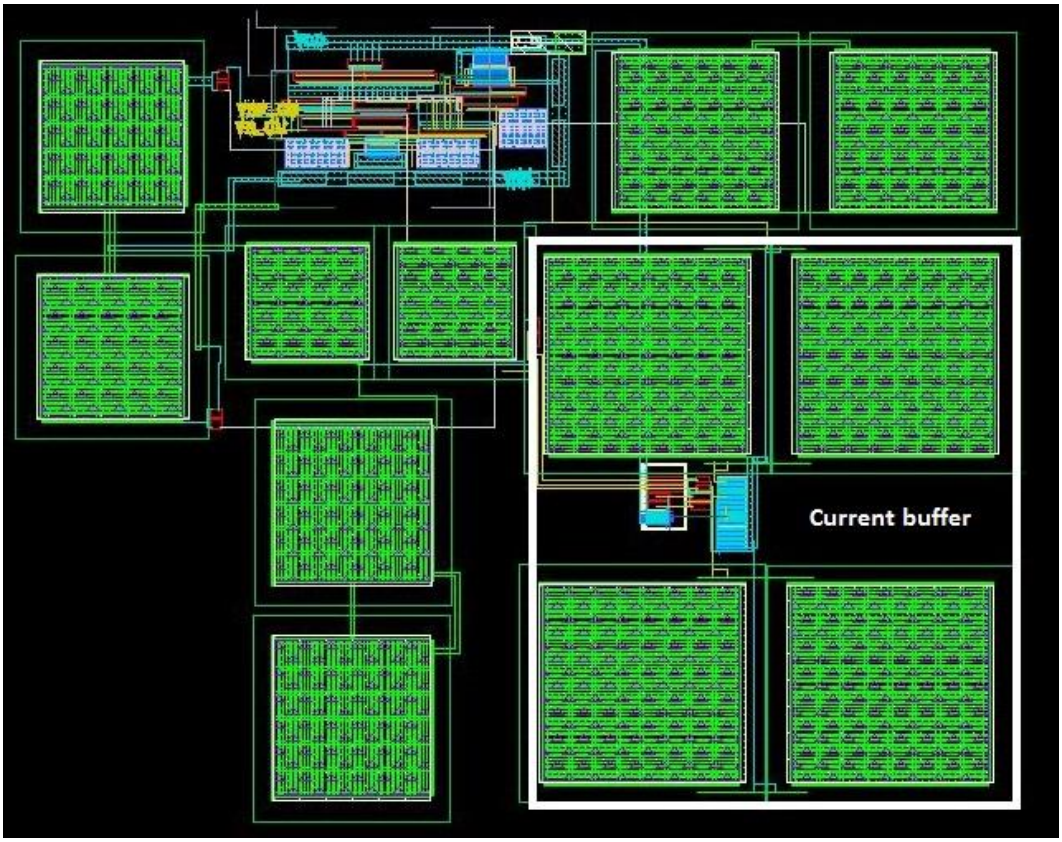

Fig. 47 Layout of the proposed baseband circuit

After the layout, effects such as parasitics from substrate capacitances or metal trace resistance can severely affect the response of the baseband circuit at higher frequencies. By following good layout techniques, these effects can be mitigated to a certain extent. In the layout of the baseband circuit, transistors have been placed in common centroid fashion or inter-digitized to reduce deviation in performance parameters because of process or temperature variations. For effective current mirroring, the transistors in the buffer circuit have been matched using common centroid technique. Figure 47 shows the CG-MINV baseband circuit layout with input capacitors. The two input capacitors have been split into four for better matching. The area of the layout is $504\mu m \times 387\mu$m. The layout of the TIA-biquad is shown Fig. 48. The OTA has been instantiated three times with the resistors and capacitors required for the third order filter structure with a total area of $495\mu m \times 332\mu m$.

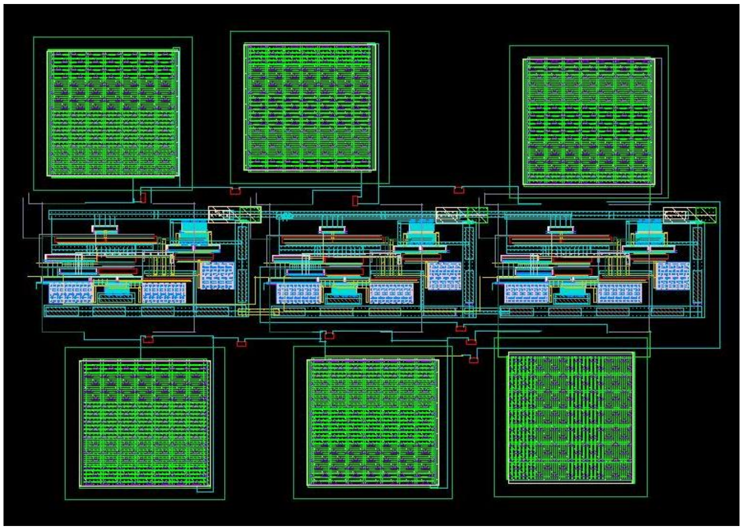

Fig. 48 Layout of the TIA-biquad circuit

In the next section, the layouts of the CG-MINV circuit has been compared with the TIA-biquad circuit for various performance metrics.

3.7 Post layout simulations

Figure 49 shows the frequency response of the baseband circuits for the baseband circuits: CG-MIV and TIA-biquad. The low frequency gain is $66dB\Omega$ and the ω_{3dB}cut-off frequency is $10MHz$ for the Butterworth lowpass filter implementation. The post-layout result is similar to the schematic simulation.

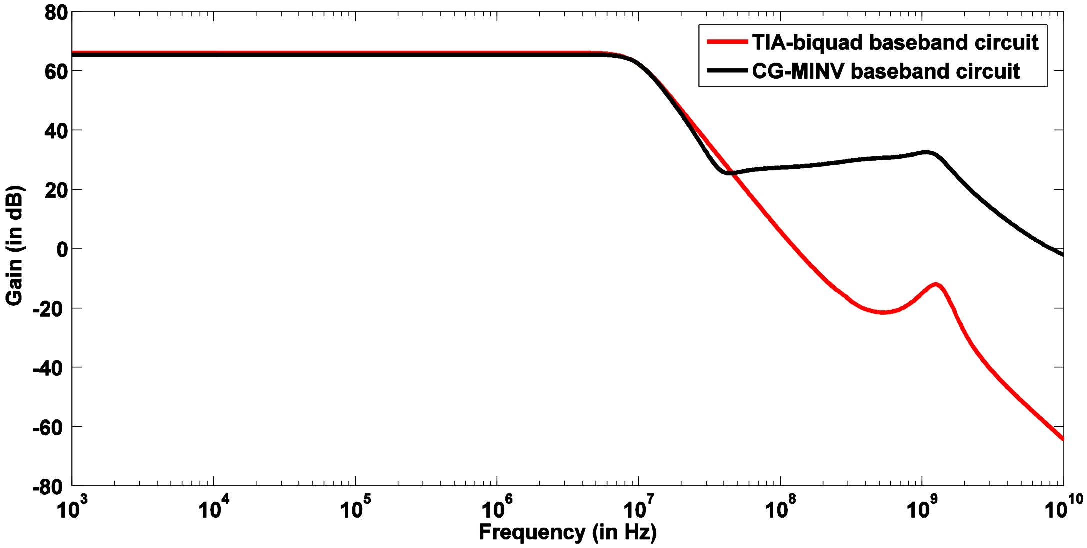

Fig. 49 Frequency response of the baseband circuits

The input impedance of the baseband circuits is plotted in the Fig. 50. We can see that the CG-MINV circuit has least peaking at high frequencies and the post-layout simulations verify the trend.

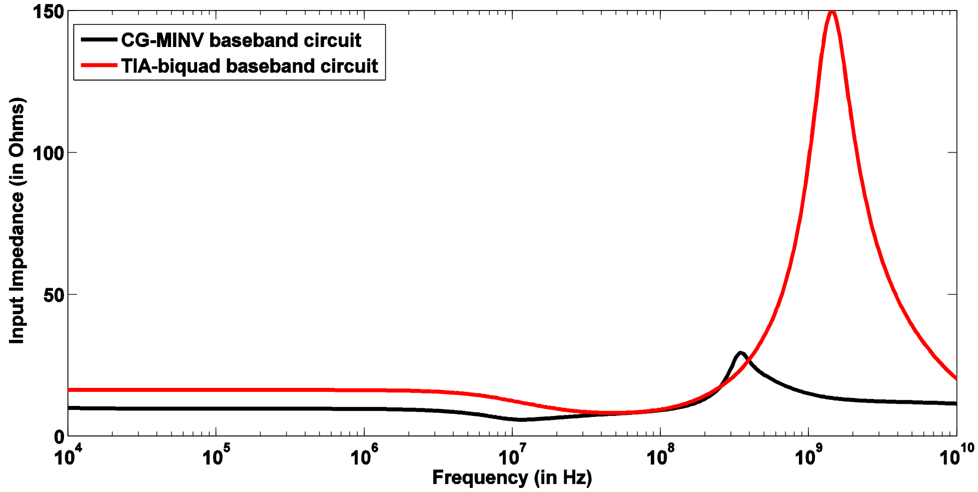

Fig. 50 Input Impedance of baseband circuits

The input-referred current noise for the baseband circuits is plotted in Fig. 51 for the layout. The integrated noise values are summarized in Table XI.

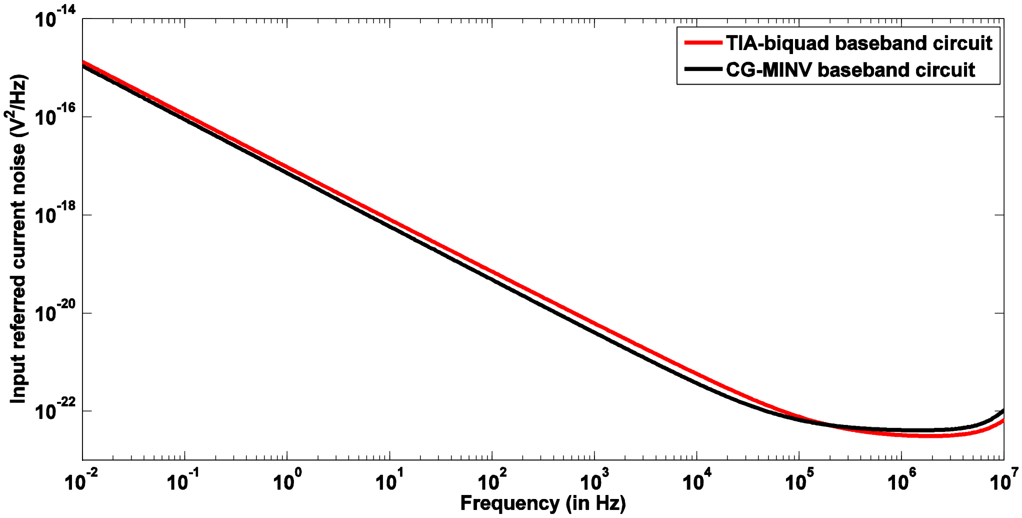

Fig. 51 Input-referred current noise for the baseband circuits

The Table XI summarizes the performance metrics for the baseband circuits. The linearity of the baseband circuit is measured by two-tone test across different frequencies along with operating range of the circuit in the same way as it was done during the schematic simulations.

Table XI Post Layout results for the baseband circuits

Parameter			**CG-MINV**	**TIA-biquad**
Low frequency gain (in dBΩ)			65.35	65.88
ω_{3dB}cut-off frequency			10.01 MHz	9.35 MHz
Linearity	F_1	F_2	IM_3 (in dB)	
	(in MHz)			
	7	9	-77.45	-81.22
	9.8	10.2	-83.74	-89.54
	10	12.5	-67.66	-72.29
	10	15	-81.23	-82.10
	10	17.5	-76.25	-73.32
	10	18	-77.49	-74.21
	30	50	-70.25	-69.12
	30	51	-78.45	-78.22
	30	52	-80.45	-80.92
	30	54	-72.01	-70.31
	30	55	-73.25	-73.67
	30	56	-82.67	-82.22
	30	57	-78.21	-78.90
	30	58	-81.45	-83.10
	60	115	-91.34	-87.92
	70	135	-93.22	-89.21
	80	155	-95.98	-89.12
	90	175	-97.32	-92.52
	100	195	-99.21	-93.01
Input-referred integrated Noise (from 0.01Hz to 10MHz)			25.90 nV	23.38 nV
Input Impedance	**At Low frequency**		09.68	16.26
	Maximum value (peaked)		29.42	149.9
Power Consumption (W)			6.17m	11.36m

Post-layout simulation results show that the CG-MINV baseband circuit has comparable linearity and noise performance with lower power consumption. The value of input-referred noise has been increased slightly due to layout parasitics. After performing the post-layout simulations with the stand-alone baseband circuit, the complete receiver has been simulated with the minimally invasive baseband circuit. Fig. 52 shows the noise figure with respect to frequency for the receiver. The noise figure shows a degradation of $2\ dB$ after the layout. However, noise figure requirements on a typical wireless network (Wi-Fi) are $14.8dB$ for $802.11b$ and $7.5dB$ for $802.11a$ and g, which are met by the designed receiver.

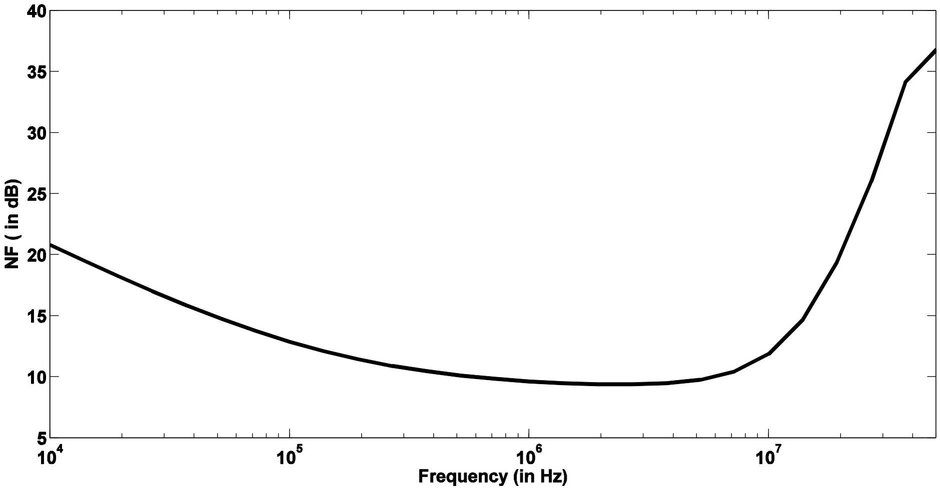

Fig. 52 Noise figure for the receiver (Post layout simulation)

Table XII Post-layout results for the receiver with CG-MINV baseband circuit

Parameter	**Value**
Conversion Gain (in dB)	25.62
Noise Figure (in dB)	9.75

In conclusion, we have compared a novel baseband circuit, which is a cascade of a common-gate current buffer and the third order minimally invasive filter with a conventional baseband circuit formed by the cascading of a first order TIA and a Tow-Thomas biquad as the second order part. The noise and linearity figures are similar to the TIA-biquad counterpart while consuming half the power consumption as the TIA-biquad circuit. The broad-band input impedance of the designed baseband circuit is 9.68 Ω, which is much lower than the input impedance of conventional circuit and becomes crucial when integrated with the broadband receiver where the mixer's performance depends on the input impedance offered to it by the baseband portion [36].

CHAPTER IV

CONCLUSION

A new concept in designing analog filters has been proposed in this work. The minimally invasive filter topology is effectively synthesis of a frequency dependent impedance, which is transparent when the input signal is in-band, while providing a low impedance path to the ground when the signal is out-of-band for the filter. The concept of a minimally invasive filter is extended to higher orders while providing detailed procedure of implementing voltage-mode lowpass minimally invasive filters. Minimally invasive filter topologies have been compared with Tow-Thomas biquad counterparts of equivalent filter orders and it has been shown that minimally invasive filters in voltage domain provide better linearity and noise at a cost of increase in area.

The idea of minimally invasive filtering is extended to current-mode and a novel current-mode baseband circuit is designed for a broad-band receiver. By using a current-mode lowpass minimally invasive filter structure, higher order filtering can be incorporated into the receiver chain, thereby relaxing the specifications on the ADC, which follows the receiver. Also, we can see that the current buffer-minimally invasive filtering based baseband circuit provides a low broad-band input impedance and a transimpedance gain of $66dB\Omega$ with an attenuation of $44dB$ at $50MHz$, while being very competitive in terms of noise and linearity with the conventional TIA based implementations while having a lower power consumption and comparable area. The input impedance of the designed baseband circuit is $9.68\ \Omega$, while the conventional TIA based baseband circuit has an input impedance of $16.26\ \Omega$ with almost twice the power consumption as the designed baseband circuit. The IM_3 plots show that the designed baseband circuit offers similar attenuation to out-of-band-blockers as the conventional third order TIA based baseband circuit at half the power consumption. Moreover, the minimally invasive circuit is a current-mode filter where the signal travels as a current throughout the baseband portion. When integrated with the receiver, we observe a slightly better linearity in presence of out-of -band blockers, which becomes very crucial for the receiver performance. In conclusion, this work establishes the concept of minimally invasive filtering and provides suitable applications wherein the idea can be viably used to improve the noise and linearity without much degradation in power or area consumed.

REFERENCES

1. Mobile and Portable DVB-T Radio Access Interface Specification, MBRAI-02-16, 1.0.
2. H. M. Geddada, C.-J. Park, H.-J. Jeon, J. Silva-Martinez, A. I. Karsilayan, and D. Garrity, “Design Techniques to Improve Blocker Tolerance of ADCs,” IEEE Transaction on VLSI Systems, 2014.
3. Saiteja Damera, Aydin I. Karsilayan and Jose Silva-Martinez, “Design of Minimally Invasive All Pole Analog Lowpass filters,” IEEE MWSCAS 2014.
4. A. Perez-Carillo, S. S. Taylor, J. Silva-Martinez, and A. I. Karsilayan, “A large-signal blocker robust transimpedance amplifier for coexisting radio receivers in 45nm cmos,” in Proc. IEEE RFIC, June 2011.
5. C. H. J. Mensink et al., “A CMOS “soft-switched” transconductor and its application in gain control and filters,” IEEE J. Solid-State Circuits, vol. 32, no. 7, pp. 989–998, Jul. 1997.
6. J. F. Fernandez-Bootello et al., “A 0.18 m CMOS low-noise elliptic low-pass continuous-time filter,” in Proc. IEEE Int. Symp. Circuits and Systems (ISCAS), May 23-26, 2005, vol. 1, pp. 800–803.
7. A. Yoshizawa et al., “A channel-select filter with agile blocker detection and adaptive power dissipation,” IEEE J. Solid-State Circuits, vol. 42, no. 5, pp. 1090–1099, May 2007.
8. C. Yoo et al., “A 1.5-V 4-MHz CMOS continuous-time filter with single-integrator based tuning,” IEEE J. Solid-State Circuits, vol. 33, no. 1, pp. 18–27, Jan. 1998.

9. H. A. Alzaher et al., “A CMOS highly linear channel-select filter for 3G multistandard integrated wireless receivers,” IEEE J. Solid-State Circuits, vol. 37, no. 12, pp. 27–37, Jan. 2002.
10. F. Krummanecher et al., “A 4-MHz CMOS continuous-time filter with on-chip automatic tuning,” IEEE J. Solid-State Circuits, vol. 32, no. 7, pp. 989–998, Jul. 1997.
11. W. Schelmbauer et al., “An analog baseband chain for a UMTS zero-IF receiver in a 75 GHz BiCMOS technology,” in IEEE MTT-S Dig. Tech. Papers, Jun. 2002, vol. 1, pp. 13–16.
12. J. Cherry et al., “On the characterization and reduction of distortion in bandpass filters,” IEEE Trans. Circuits Syst., vol. 45, no. 5, pp. 523–537, May 1998.
13. S. D’Amico et al., “A 4.1-mW 10-MHz fourth-order source-follower based continuous-time filter with 79-dB DR,” IEEE J. Solid-State Circuits, vol. 41, no. 12, pp. 2713–2719, Dec. 2006.
14. A. Antoniou, “Realization of gyrators using operational amplifiers, and their use in RC-active network synthesis,” in Proc. Inst. Elect. Eng., Nov. 1969, vol. 116, pp. 1838–1850.
15. S. Kousai et al., “A 19.7 MHz, fifth-order active-RC Chebyshev LPF for draft IEEE802.11n with automatic quality-factor tuning scheme,” IEEE J. Solid-State Circuits, vol. 42, no. 11, pp. 2326–2337, Nov. 2007.

16. A. Antoniou, “Bandpass transformation and realization using frequency-dependent negative resistance elements,” IEEE Trans. Circuit Theory, vol. CT-18, pp. 297–299, Mar. 1971.
17. K. Martin et al., “Optimum design of active filters using the generalized immitance converter,” IEEE Trans. Circuits Syst., vol. CAS-24, pp. 495–502, Sep. 1977.
18. L. T. Bruton, “Network transfer functions using the concept of frequency dependent negative resistance,” IEEE Trans. Circuit Theory, vol. CT-16, pp. 406–408, Aug. 1969.
19. J. Hutchison et al., “Some notes on practical FDNR filters,” IEEE Trans. Circuits Syst., vol. CAS-28, pp. 242–245, Mar. 1981.
20. L. T. Bruton et al., “Electrical noise in low-pass FDNR filters,” IEEE Trans. Circuit Theory, vol. CT-20, pp. 154–158, Mar. 1973.
21. N. C. Bui et al., “On antoniou’s method for bandpass filters with FDNR and FDNC elements,” IEEE Trans. Circuits Syst., vol. CAS-25, pp. 169–172, Mar. 1978.
22. A. Tekin, H. Elwan, A. Ismail, and K. Pedrotti, “Noise-Shaping Gain-Filtering Techniques for Integrated Receivers,” IEEE Journal of Solid-State Circuits, vol. 44, no. 10, pp. 2689–2701, Oct. 2009.
23. B. Razavi, *RF Microelectronics*, Upper Saddle River, NJ: Prentice Hall, 1998.
24. H. Darabi and A. Abidi, “Noise in RF-CMOS mixers: A simple physical model,” *IEEE J. Solid-State Circuits*, vol. 35, no. 1, pp. 15–25, Jan. 2000.

25. W. Redman-White, D. M. Leenaerts, and W. Leenaerts, “1/f noise in passive CMOS mixers for low and zero IF integrated receivers,” in *Proc. Eur. Solid-State Circuits Conf.*, Sep. 2001, pp. 41–44.
26. B. Razavi, Design of Analog CMOS Integrated Circuits. McGraw-Hill, 2001.
27. Jusung Kim and Jose Silva-Martinez, “Low-Power, Low-Cost CMOS Direct-Conversion Receiver Front-End for Multistandard Applications”, IEEE Journal of solid-state circuits, Vol 48, No .9, September 2013.
28. R. Bagheri, A. Mizraei, S. Chehrazi, M. E. Heidari, M. Lee, M. Mikhemar, W. Tang, and A. Abidi, “An 800-MHz–6 GHz software- defined wireless receiver in 90-nm CMOS,” IEEE J. Solid-State Circuits, vol. 41, no. 12, pp. 2860–2876, Dec. 2006.
29. S. C. Blaakmeer, E. A. M. Klumperink, D. M. W. Leenaerts, and B. Nauta, “THE BLIXER a wideband Balun-LNA-I/Q-Mixer topology,” IEEE J. Solid-State Circuits, vol. 43, no. 12, pp. 2706–2715, Dec. 2008.
30. N. Poobuapheun, W.-H. Chen, Z. Boos, and A. M. Kiknezad, “A 1.5-V 0.7–2.5 GHz CMOSquadrature demodulator formultiband direct-conversion receivers,” IEEE J. Solid-State Circuits, vol. 42, no. 8, pp. 1669–1677, Aug. 2007.
31. A. Amer, E. Hegazi, and H. F. Ragaie, “A 90-nm wideband merged CMOS LNA and mixer exploiting noise cancellation,” IEEE J. Solid- State Circuits, vol. 42, no.2, pp. 323–328, Feb. 2007.

32. N. Kim, V. Aparin, and L. E. Larson, “A resistively degenerated wideband passive mixer with low noise figure and high ,” IEEE Trans. Microw. Theory Tech., vol. 58, no. 4, pp. 820–830, Apr. 2010.

33. Chih-Fan Liao; Shen-Iuan Liu, "40 Gb/s Trans-impedance-AGC Amplifier and CDR Circuit for Broadband Data Receivers in 90 nm CMOS," *Solid-State Circuits, IEEE Journal of*, vol.43, no.3, pp.642, 655, March 2008.

34. Chenglin Cui; Tae-Sung Kim; Seong-Kyun Kim; Jun-Kyung Cho; Su-Tae Kim; Byung Sung Kim, "Effects of the nonlinearity of the common-gate stage on the linearity of CMOS cascode low noise amplifier, "*Radio Frequency Integrated Circuits Symposium (RFIC), 2011 IEEE* , vol., no., pp.1,4, 5-7 June 2011.

35. B. K. Thandri and J. Silva-Martinez, “A robust feedforward compensation scheme for multistage operational transconductance amplifiers with no miller capacitors,” IEEE J. Solid-State Circuits, vol. 38, no. 2,pp. 237–243, Feb. 2003.

36. H. Khatri, P. S. Gudem, and L. E. Larson, “Distortion in current commutating passive CMOS downconversion mixers,” *IEEE Trans. Microw.Theory Tech.*, vol. 57, no. 11, pp. 2671–2681, Nov. 2009.

APPENDIX A

PARAMETRIC AND CORNER SIMULATIONS

All the simulations in Appendix A are done using TSMC 0.13μm technology. Results show the impact of process and temperature variations on the baseband circuit.

Frequency response of the baseband circuit

Figure A.1 shows the frequency response of the designed baseband circuit at both schematic and layout level when temperature is varied from -40°C to 100°C while the power supply varies from 1.1 V to 1.3 V (10% variation in power supply at a nominal voltage of 1.2 V).

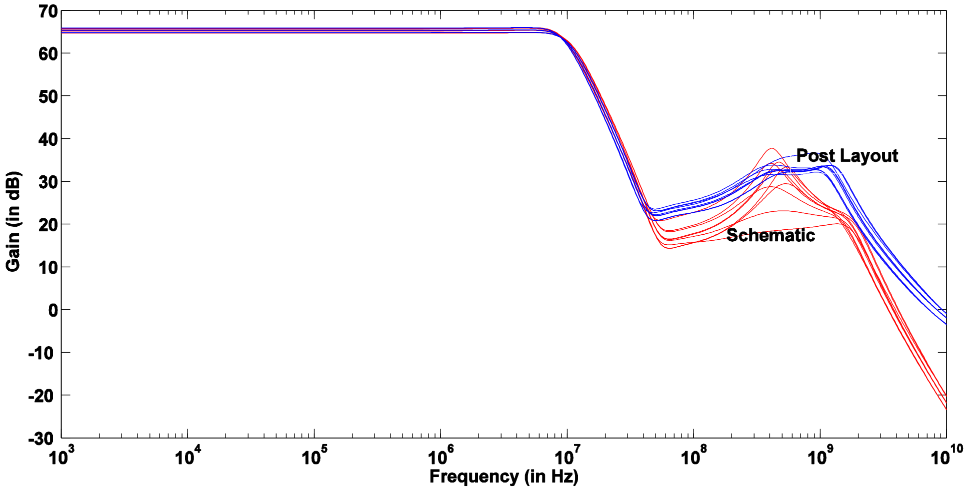

Fig. A. 1 Frequency response variation of the baseband circuit

Integrated Input-referred noise of the baseband circuit

Figure A.2 shows the integrated input-referred current noise of the designed baseband circuit (integrated from $0.01Hz$ to $10MHz$) at both schematic and layout level when temperature is varied from -40°C to 100°C while the power supply varies from 1.1 V to 1.3 V (10% variation in power supply at a nominal voltage of 1.2 V). We can see that the thermal noise dominates for the designed baseband circuits because the noise increases with increase in temperature along X-axis. The layout shows slightly higher integrated noise because of layout parasitics.

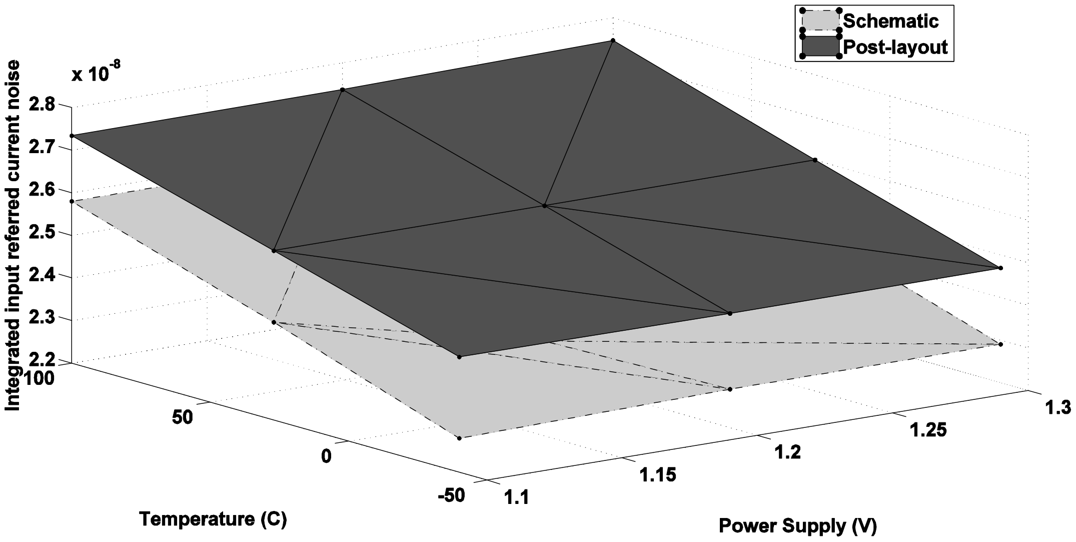

Fig. A. 2 Noise variation of the baseband circuit

Input Impedance of the baseband circuit

The layout of the baseband circuit is subjected to voltage and temperature variations similar to the previous section and the input impedance is plotted with respect to frequency in Fig. A.3.

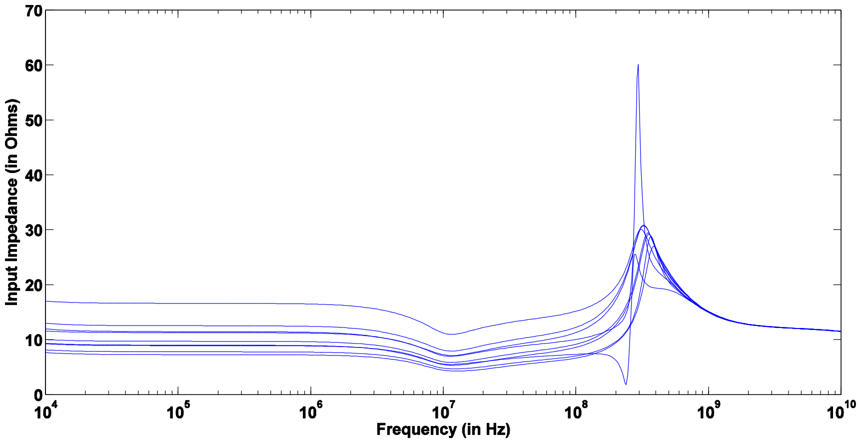

Fig. A. 3 Input impedance variation for the baseband circuit

With voltage and temperature variations, we can see that the input impedance has a maximum value of around 60 Ω in the frequency band for the minimally invasive baseband circuit, which is still less than the input impedance offered by a conventional solution as discussed in previous chapter.